

Tangencies between global invariant manifolds and slow manifolds near a singular Hopf bifurcation

José Mujica, Bernd Krauskopf and Hinke M. Osinga

Department of Mathematics, The University of Auckland, Private Bag 92019, Auckland, New Zealand

email: J.Mujica@auckland.ac.nz, B.Krauskopf@auckland.ac.nz, H.M.Osinga@auckland.ac.nz

Abstract

Invariant manifolds of equilibria and periodic orbits are key objects that organise the behaviour of a dynamical system both locally and globally. If multiple time scales are present in the dynamical system, there also exist so-called slow manifolds, that is, manifolds along which the flow is very slow compared with the rest of the dynamics. In particular, slow manifolds are known to organise the number of small oscillations of what are known as mixed-mode oscillations (MMOs). Slow manifolds are locally invariant objects that may interact with invariant manifolds, which are globally invariant objects; such interactions produce complicated dynamics about which only little is known from a few examples in the literature. We study the transition through a quadratic tangency between the unstable manifold of a saddle-focus equilibrium and a repelling slow manifold in a system where the corresponding equilibrium point undergoes a supercritical singular Hopf bifurcation. We compute the manifolds as families of orbits segments with a two-point boundary value problem setup and track their intersections, referred to as connecting canard orbits, as a parameter is varied. We describe the local and global properties of the manifolds, as well as the role of the interaction as an organiser of large-amplitude oscillations in the dynamics. We find and describe recurrent dynamics in the form of MMOs, which can be continued in parameters to Shilnikov homoclinic bifurcations. We detect and identify two such homoclinic orbits and describe their interactions with the MMOs.

1 Introduction

In many areas of application one encounters behaviour that is characterised by dynamics with slow and fast episodes; well-known examples are chemical reactions, non-harmonic oscillations, spiking and bursting [9, 24, 25, 27, 37]. Their mathematical description leads to vector-field models, called slow-fast systems, that have state variables separated into groups that evolve on different time scales. In the simplest case there is one group of slow and one group of fast variables, with a parameter determining the ratio between the two time scales. Geometric singular perturbation theory [2, 7, 13, 14, 26], introduced by Fenichel in the 1970s, exploits this splitting of time scales by constructing actual trajectories from concatenations of slow and fast segments that exist in the respective limits of the slow and fast dynamics. This approach has been very successful in explaining complex oscillations when there is a single slow variable [3, 20, 24, 38]. More recently, there has been a lot of interest in understanding the

dynamics of systems with two slow variables [6, 7, 17, 18, 22, 33, 37, 46, 47]. Key objects here are attracting and repelling slow manifolds, which are surfaces in phase space that govern the slow motion of trajectories.

We are particularly interested in three-dimensional slow-fast systems with two slow and one fast variables. Such systems are known to exhibit mixed-mode oscillations (MMOs), which are characterised by an alternation of both small and large-amplitude oscillations (SAOs and LAOs, respectively). There are several studies providing mechanisms that give rise to the SAOs [7, 8, 9, 10, 16, 22, 47], including passage near special points in phase space called folded singularities and oscillations arising from a so-called singular Hopf bifurcation. As a specific example, we consider the vector field introduced by Guckenheimer in [7, 16, 22] that is given by the system of differential equations

$$\begin{cases} \varepsilon \dot{x} &= y - x^2 - x^3, \\ \dot{y} &= z - x, \\ \dot{z} &= -\nu - ax - by - cz, \end{cases} \quad (1)$$

with $a, b, c, \nu \in \mathbb{R}$ and $0 < \varepsilon \ll 1$. System (1) exhibits MMOs for which the SAOs are organised by a singular Hopf bifurcation [5, 7, 16, 22]. This is a Hopf bifurcation [35] that involves both slow and fast variables and is characterised by a rapid growth in the amplitude of the emanating periodic orbit. The study in [7] identifies in system (1) a tangency between a two-dimensional repelling slow manifold and a two-dimensional global invariant manifold associated with the equilibrium involved in the singular Hopf bifurcation; see also [16] and [22], where a different model is used. The tangency was obtained locally by computing selected backward trajectories of the repelling slow manifold and forward trajectories of the invariant manifold up to a suitable two-dimensional section. We are interested in the global consequences of such a tangency, which requires the calculation of the respective slow manifold and invariant manifold as global surfaces in phase space. Throughout this paper, we use the same parameter values as in [7] for which the tangency was found, namely, $a = 0.008870, b = -0.5045, c = 1.17$ and $\varepsilon = 0.01$, and consider ν as the bifurcation parameter.

Figure 1(a) shows a one-parameter bifurcation diagram of system (1) for $\nu \in (-0.6, 1.4)$. Here, the variable x is plotted on the vertical axis with the parameter ν on the horizontal axis. The black curve represents equilibria of system (1). The upper and lower branches correspond to saddle equilibria with one unstable eigenvalue and two stable real ones. These branches collide with the middle branch in saddle-node bifurcations for $\nu = \nu_{\text{SN}}^L \approx -0.416$ and $\nu = \nu_{\text{SN}}^R \approx 1.277$, respectively. The middle branch corresponds to points $p = p(\nu) := (x_\nu, x_\nu^2 + x_\nu^3, x_\nu)$, where x_ν is the root nearest to 0 of the equation

$$\nu + (a + c)x_\nu + bx_\nu^2 + bx_\nu^3 = 0,$$

for $\nu \in (\nu_{\text{SN}}^L, \nu_{\text{SN}}^R)$. The equilibrium p is unstable for $\nu_{\text{H}}^L \leq \nu \leq \nu_{\text{H}}^R$, where $\nu_{\text{H}}^L \approx -8.587 \times 10^{-5}$ and $\nu = \nu_{\text{H}}^R \approx 0.8607$ are supercritical singular Hopf bifurcation points. Both singular Hopf bifurcations give rise to the same family of periodic orbits Γ_ν of system (1). The green curve in Figure 1(a) corresponds to the maximum value of the x -coordinate of Γ_ν for $\nu \in (\nu_{\text{H}}^L, \nu_{\text{H}}^R)$. After the singular Hopf bifurcation at $\nu = \nu_{\text{H}}^L$, as ν increases, there is a very small interval where the amplitude of Γ_ν grows in a square-root fashion, as is to be expected near a Hopf bifurcation [35]. The amplitude then grows extremely rapidly, a phenomenon that is known as a canard explosion, until it reaches a plateau that corresponds to relaxation oscillations. The same phenomenon occurs near $\nu = \nu_{\text{H}}^R$ when ν decreases; see panels (b1) and (c1) of Figure 1. The stable periodic orbit Γ_ν that emanates from the supercritical singular Hopf bifurcation becomes unstable in a period-doubling bifurcation and becomes stable again after

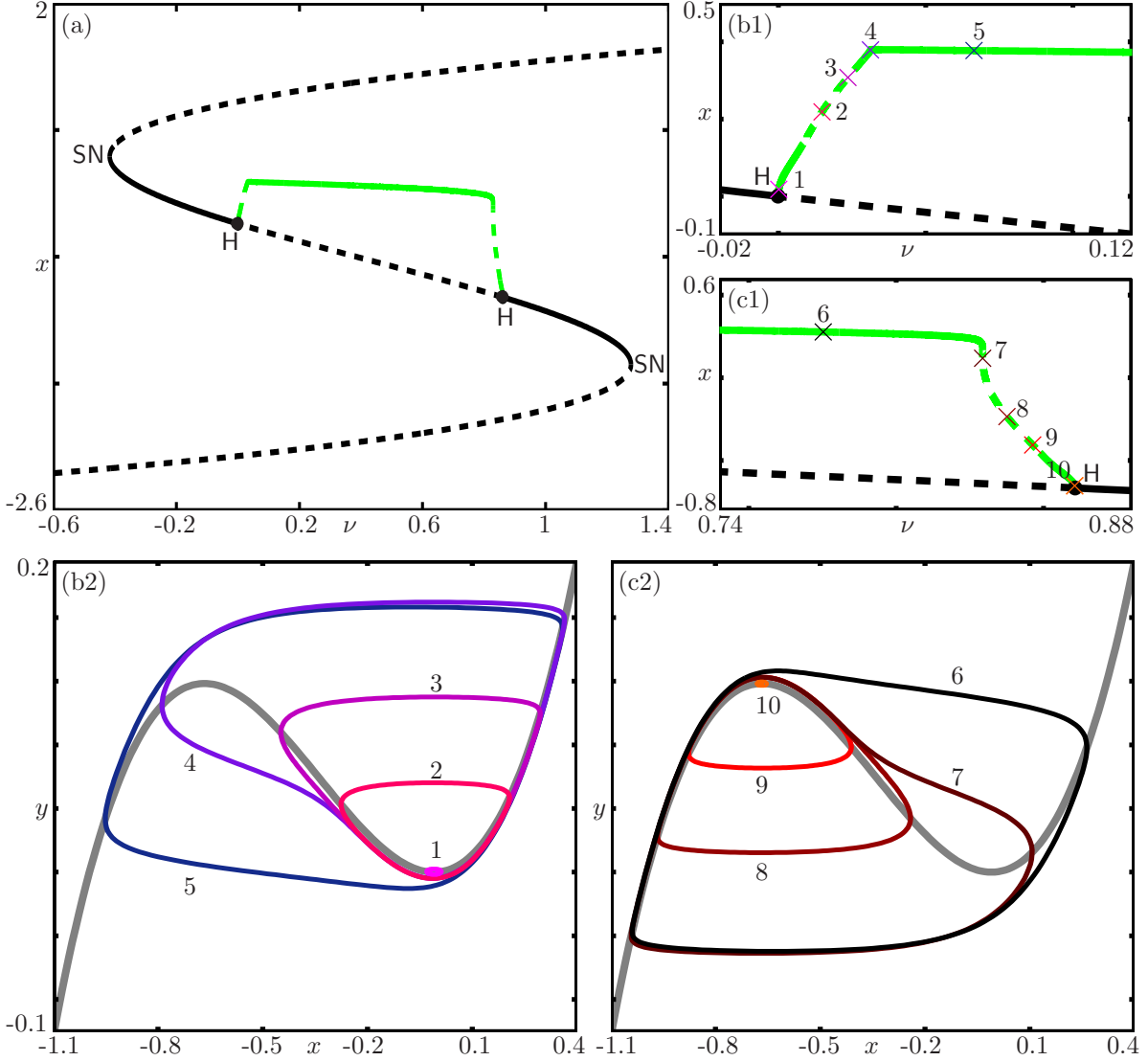


Figure 1: One-parameter bifurcation diagram of system (1) for $\nu \in (-0.6, 1.4)$. Panels (b1) and (c1) show enlargements of panel (a) near the Hopf bifurcations. The corresponding panels (b2) and (c2) show the projections on the (x, y) -plane of a selection of periodic orbits, as indicated by the numbered crosses in panels (b1) and (c1), respectively.

another period-doubling bifurcation; the stability of Γ_ν does not change during the relaxation oscillations. The numbered crosses on the curve of periodic orbits in panels (b1) and (c1) correspond to the periodic orbits displayed in panels (b2) and (c2), respectively; here, the periodic orbits are shown projected onto the (x, y) -plane together with (the projection of) the x -nullcline (thick gray curve).

For $\nu \in (\nu_H^L, \nu_H^R)$, the saddle-focus p has one stable real eigenvalue and a pair of unstable complex-conjugate eigenvalues. According to the Stable Manifold Theorem [19, 35, 40], the equilibrium point p has a one-dimensional stable manifold $W^s(p)$ and a two-dimensional unstable manifold $W^u(p)$, which are defined as

$$\begin{aligned} W^s(p) &:= \{q \in \mathbb{R}^3 : \varphi^t(q) \rightarrow p \text{ when } t \rightarrow \infty\}, \\ W^u(p) &:= \{q \in \mathbb{R}^3 : \varphi^t(q) \rightarrow p \text{ when } t \rightarrow -\infty\}, \end{aligned}$$

where φ^t denotes the flow of the vector field (1). The sets $W^s(p)$ and $W^u(p)$ are immersed

manifolds that are as smooth as the vector field and tangent at p to the associated stable and unstable linear eigenspaces $E^s(p)$ and $E^u(p)$, respectively.

In the parameter regime where $W^u(p)$ exists, there also exist attracting and repelling slow manifolds S_ε^a and S_ε^r , which are associated with the slow motion of trajectories of system (1); these are surfaces in the three-dimensional phase space that organise the slow-fast nature of the system globally. Their existence is guaranteed by Fenichel theory [13, 14, 26]. These new types of manifolds are formally introduced in Section 2.

Two-dimensional slow manifolds and global invariant manifolds can be computed reliably with recently developed numerical methods [15, 20, 23, 30, 31]. Our approach is based on the continuation of solutions to a two-point boundary value problem, and it is implemented in AUTO [11]. One of the benefits of this approach is that it gives reliable results even in the presence of the extreme sensitivity with respect to initial conditions, which is an important feature of slow-fast systems. Our setup allows us to calculate slow manifolds for $\varepsilon > 0$ away from the singular limit when ε is not necessarily very small. Moreover, we are able to extend slow manifolds past regions containing points where normal hyperbolicity is lost. We take advantage of the flexibility of this computational technique to calculate the respective manifolds themselves, as well as their intersection sets with suitable two-dimensional surfaces.

The main goal of this paper is to study the global effect of the interaction of $W^u(p)$ with the (extended) repelling slow manifold S_ε^r on the dynamics of system (1). We compute and visualise the respective manifolds and analyze the consequences for the dynamics of their interaction both from a local and a global point of view. We find that S_ε^r wraps around $W^s(p)$ in backward time. In the parameter regime that we consider, $W^u(p)$ accumulates in forward time on, and is bounded by the attracting periodic orbit Γ_ν . As soon as $W^u(p)$ interacts with S_ε^r , it is forced to make large excursions into phase space before accumulating on Γ_ν . As a consequence, $W^u(p)$ scrolls around Γ_ν and returns back to itself as it comes close to $W^s(p)$. This return creates secondary intersections between S_ε^r and $W^u(p)$, which have not been studied previously. Furthermore, this global interaction gives rise to a one-parameter family of periodic MMOs that are linked with Γ_ν . These new periodic MMOs are not part of the family of periodic orbits created at the singular Hopf bifurcation shown in Figure 1. We also identify Shilnikov homoclinic orbits as organising centres for the dynamics of system (1).

This paper is organised as follows. Section 2 reviews the necessary theory of slow-fast systems and defines the repelling slow manifold S_ε^r studied here. Section 3 describes the interaction between $W^u(p)$ and the repelling slow manifold, both from a local and global point of view; here, we focus on the transition through a quadratic tangency between these two manifolds as ν varies. How the initial tangency leads to secondary tangencies and intersections that organise the global returns is presented in Section 4. Section 5 shows the existence of two periodic MMOs, linked with the attracting periodic orbit Γ_ν , in a parameter regime where secondary interactions between the repelling slow manifold and $W^u(p)$ take place. The existence of Shilnikov homoclinic bifurcations of MMOs is discussed in Section 6. We end with a discussion in Section 7. Furthermore, the Appendix provides some details of the numerical techniques used in this paper.

2 Slow-fast systems

We now present some background on the slow-fast system (1) as needed for this paper. For further details, we refer the interested reader to, for example, [2, 7, 13, 14, 26, 34].

System (1) is a slow-fast system. The variable $x \in \mathbb{R}$ is fast, the variables $y, z \in \mathbb{R}$ are slow and $0 < \varepsilon \ll 1$ represents the ratio of time scales. Solutions of slow-fast systems can be thought of as a concatenation of slow motion with fast segments. Considering system (1) for $\varepsilon = 0$ gives the reduced system

$$\begin{cases} 0 &= y - x^2 - x^3, \\ \dot{y} &= z - x, \\ \dot{z} &= -\nu - ax - by - cz \end{cases}$$

for the limiting slow motion. It is a differential-algebraic equation (DAE) where the constraint on the first equation defines the critical manifold

$$S := \{(x, y, z) \in \mathbb{R}^3 \mid y - x^2 - x^3 = 0\},$$

which is the nullcline of the fast variable x . For system (1), the critical manifold S does not depend on z , so it is a surface for which every cross-section with z constant is the gray S-shaped curve shown in panels (b2) and (c2) of Figure 1.

The dot in system (1) represents differentiation with respect to time on the slow time scale. One can rewrite system (1) with respect to the fast time scale via a time rescaling by ε to obtain

$$\begin{cases} x' &= y - x^2 - x^3, \\ y' &= \varepsilon(z - x), \\ z' &= \varepsilon(-\nu - ax - by - cz), \end{cases} \quad (2)$$

where the prime denotes the derivative with respect to time on the fast time scale. Fast segments of solutions of system (1) are approximated by solutions of the fast subsystem or layer equations

$$\begin{cases} x' &= y - x^2 - x^3, \\ y' &= 0, \\ z' &= 0, \end{cases}$$

which is a family of differential equations on the fast time scale, obtained as the singular limit of system (2) for $\varepsilon = 0$. Here the x' -equation depends on y , which is now a parameter. Note that the critical manifold is a manifold of equilibria for the fast subsystem. In fact, all equilibria of a slow-fast system lie on its critical manifold and are also equilibria of the fast subsystem.

Since system (1) has a single fast variable, the critical manifold has portions that are either attracting or repelling. More precisely, S has two attracting sheets

$$S^{a,-} := S \cap \{x < -\frac{2}{3}\} \quad \text{and} \quad S^{a,+} := S \cap \{x > 0\},$$

and one repelling sheet

$$S^r := S \cap \{-\frac{2}{3} < x < 0\},$$

which meet at the fold curves $F^- := S \cap \{x = -\frac{2}{3}\}$ and $F^+ := S \cap \{x = 0\}$. Hence, S is an S-shaped surface that is folded with respect to the fast variable x along F^+ and F^- .

For $\varepsilon > 0$ but small enough, Fenichel Theory [13, 14] ensures the existence of attracting and repelling slow manifolds $S_\varepsilon^{a,\pm}$ and S_ε^r that are smooth $O(\varepsilon)$ perturbations of the sheets $S^{a,\pm}$ and S^r of the critical manifold S away from fold curves F^\pm . Trajectories of the full system (1) with $\varepsilon > 0$ are attracted to $S_\varepsilon^{a,\pm}$ and repelled from S_ε^r in forward time at fast exponential rates; trajectories that lie on a slow manifold remain slow for an $O(1)$ time on the slow time scale. In contrast to standard invariant manifolds, slow manifolds are locally invariant objects; this finite-time invariance, caused by the presence of different time scales, allows orbits on a slow manifold to leave along fast fibers. In this paper we study global features of the slow-fast nature and the associated return mechanism as encoded by the slow manifold S_ε^r , which we compute as an (extended) manifold formed by families of trajectory segments that are slow near S^r . Since our numerical setup extends the slow manifold past the folds of the critical manifold we are able to determine the global properties of S_ε^r as a surface in the three-dimensional phase space and how it interacts with the global invariant manifold $W^u(p)$; see the appendix for more details on our numerical setup.

3 First tangency between S_ε^r and $W^u(p)$

A first tangency between S_ε^r and $W^u(p)$ occurs at $\nu = \nu^* \approx 0.007056$. We first focus on the associated local dynamics near p as ν varies from 0.007 to 0.00712 through the tangency. We then consider the global picture arising from the interaction.

3.1 Local picture near the equilibrium p

Throughout this paper, the two-dimensional repelling slow manifold S_ε^r is represented as a blue surface, the two-dimensional unstable manifold $W^u(p)$ as a red surface and the one-dimensional stable manifold $W^s(p)$ as a light blue curve. To illustrate the nature of their interaction, we consider also their intersection sets with three local two-dimensional sections Σ_1 , Σ_2 and Σ_3 that remain fixed as ν varies. Section $\Sigma_1 \subset \{y = 0.03\}$ is chosen transverse to S_ε^r and lies between the fold curves F^\pm ; sections $\Sigma_2 \subset \{z = -0.007\}$ and $\Sigma_3 \subset \{z = -0.0017\}$ are chosen transverse to either branch of the one-dimensional stable manifold $W^s(p)$. Additionally, for $i, j = 1, 2, 3$, we introduce the map

$$\pi_{ij}^+ : \Sigma_i \mapsto \Sigma_j,$$

which maps points in Σ_i under the flow φ^t to their first intersection with Σ_j in forward time. Similarly,

$$\pi_{ij}^- : \Sigma_i \mapsto \Sigma_j$$

maps points in Σ_i under the flow φ^t to their first intersection with Σ_j in backward time. The maps π_{ij}^\pm are not defined at every point of Σ_i but are local diffeomorphisms in their respective domains of definition. For convenience of notation, we define the image of a set $X \subset \Sigma_i$ as $\pi_{ij}^\pm(X) := \{\pi_{ij}^\pm(x) : x \in X \cap D(\pi_{ij}^\pm)\}$, where $D(\pi_{ij}^\pm)$ denotes the domain of definition of π_{ij}^\pm .

Figure 2 shows in panel (a) the relative positions of S_ε^r , $W^u(p)$, $W^s(p)$ near p before the first tangency between S_ε^r and $W^u(p)$ for $\nu = 0.007$, together with sections Σ_1 , Σ_2 and Σ_3 . In order to describe the dynamics near p , we consider the intersection sets of $W^u(p)$ and S_ε^r with Σ_1 , denoted by a hat over the respective symbols, and investigate how they are mapped in backward time to Σ_2 and Σ_3 by π_{12}^- and π_{13}^- , respectively. We show in panels (a) and (b) of Figure 2 a local segment \widehat{W}_1 of the first intersection set of $W^u(p)$ with Σ_1 . Throughout this section, we consider only the local segment of \widehat{W}_1 , but note that the full first intersection set of $W^u(p)$ with Σ_1 is larger; it is presented in Section 4.1. The parabola-shaped curve \widehat{W}_1 shown

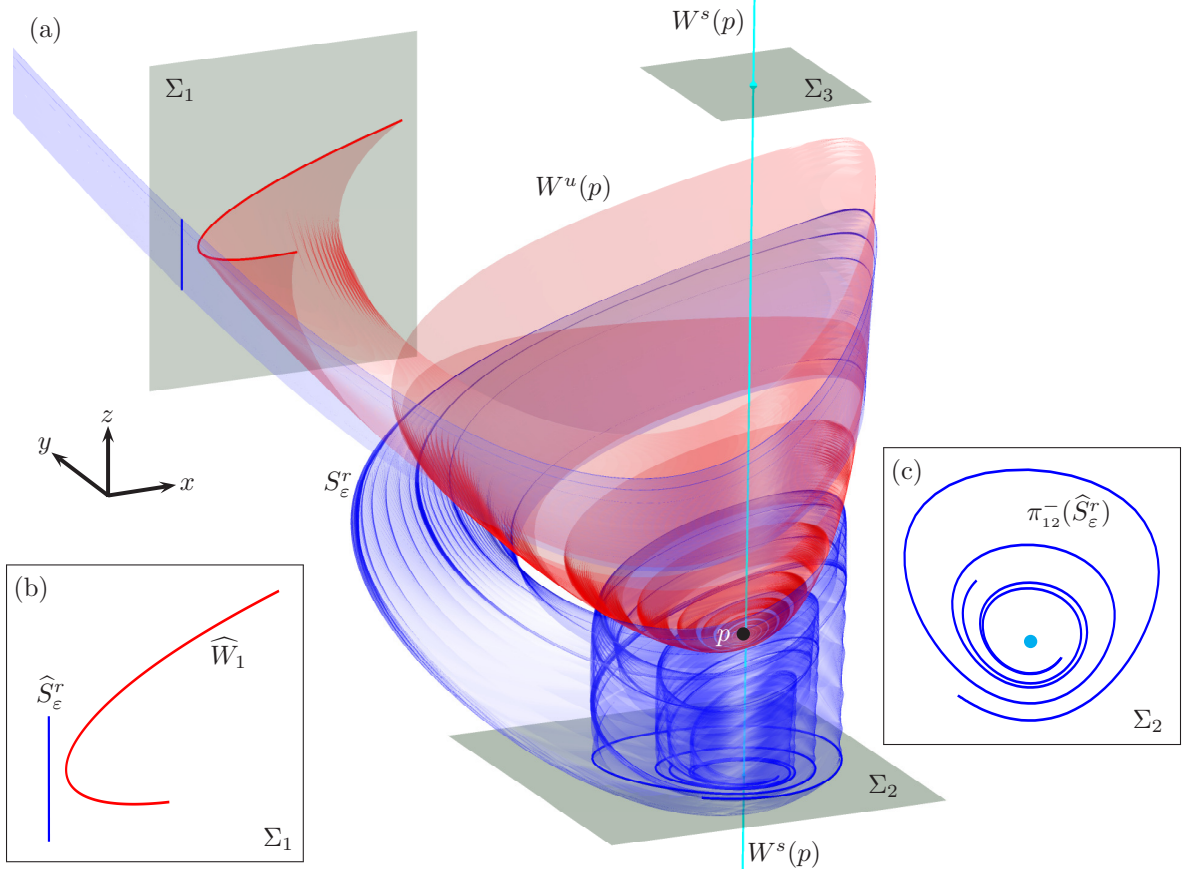


Figure 2: Interaction between S_ε^r (blue surface) and $W^u(p)$ (red surface) of system (1) with $\nu = 0.007$ before a tangency. Panel (a) shows the manifolds in (x, y, z) -space and panels (b) and (c) show their intersection curves with sections Σ_1 and Σ_2 , respectively. The equilibrium p (black dot) lies near the bottom of $W^u(p)$ and its one-dimensional stable manifold $W^s(p)$ is formed by the two light-blue curves.

in Figure 2 locally forms the boundary between $D(\pi_{12}^-)$ and $D(\pi_{13}^-)$. As panel (b) shows, the intersection set $\widehat{S}_\varepsilon^r$ of S_ε^r with Σ_1 is locally an approximately straight line that lies entirely in $D(\pi_{12}^-)$. Hence, it is mapped by π_{12}^- to Σ_2 while $\pi_{13}^-(\widehat{S}_\varepsilon^r) = \emptyset$. Geometrically, this means that S_ε^r is a band that crosses Σ_1 and then follows $W^u(p)$ spiralling towards p , due to the existence of complex-conjugate eigenvalues of the Jacobian matrix at the point p . As S_ε^r approaches p in backward time, it is pushed down and spirals around $W^s(p)$ as it intersects Σ_2 . The corresponding intersection set $\pi_{12}^-(\widehat{S}_\varepsilon^r)$ shown in panel (c), is a single curve that spirals in and back out, as S_ε^r is stretched and folded during the passage near p . The end points of $\pi_{12}^-(\widehat{S}_\varepsilon^r)$ correspond to the trajectories that bound the computed segment of S_ε^r .

The moment of the tangency, at $\nu = \nu^*$, is shown in Figure 3, with panel (a) displaying the same view shown in Figure 2(a) of the manifolds in (x, y, z) -space. The tangency between S_ε^r and $W^u(p)$, as found in [7], is best observed in Σ_1 . Figure 3(b) shows that there is a quadratic tangency between the intersection sets $\widehat{S}_\varepsilon^r$ and \widehat{W}_1 at the point $\hat{\zeta}^*$ in Σ_1 . The existence of $\hat{\zeta}^* \in \Sigma_1$ means that $\widehat{S}_\varepsilon^r$ intersects the boundary of $D(\pi_{12}^-)$ and $D(\pi_{13}^-)$ and almost every point of $\widehat{S}_\varepsilon^r$ still lies on $D(\pi_{12}^-)$, so S_ε^r does not intersect Σ_3 yet. The intersection point $\hat{\zeta}^*$ is the only point of $\widehat{S}_\varepsilon^r$ that does not lie in $D(\pi_{12}^-)$, and it corresponds to the isolated trajectory $\zeta^* \subset S_\varepsilon^r \cap W^u(p)$ (orange curve), which converges to p in backward time. We refer to ζ^* as a connecting canard orbit because it possesses some of the characteristics of a canard orbit obtained as the intersection

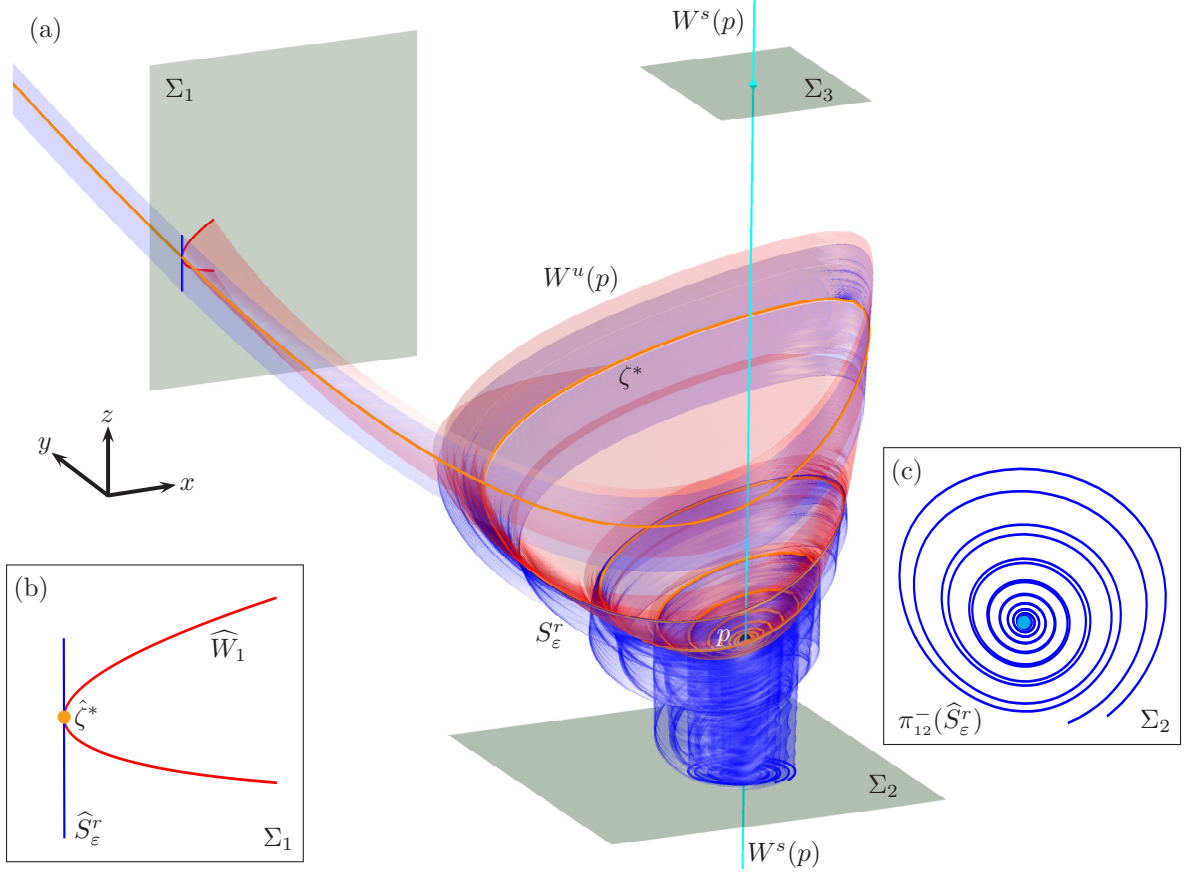


Figure 3: First tangency between S_ε^r (blue surface) and $W^u(p)$ (red surface) along the connecting canard orbit ζ^* (orange) of system (1) with $\nu = \nu^* \approx 7.056 \times 10^{-3}$. Panel (a) shows the manifolds in (x, y, z) -space and panels (b) and (c) show their intersection curves with sections Σ_1 and Σ_2 , respectively. The equilibrium p (black dot) lies near the bottom of $W^u(p)$ and its one-dimensional stable manifold $W^s(p)$ is formed by the two light-blue curves; compare with Figure 2.

between an attracting and a repelling slow manifold [46, 47]. Specifically, ζ^* remains on S_ε^r for an $O(1)$ time on the slow time scale. In fact, the connecting canard orbit ζ^* stays on S_ε^r for an arbitrary long time. The existence of ζ^* means that S_ε^r remains closer to $W^u(p)$ than before the tangency, and the stretching, folding and spiralling of S_ε^r around $W^s(p)$ in backward time is much stronger. Panel (c) shows that, since ζ^* approaches p when $t \rightarrow -\infty$, the intersection set $\pi_{12}^-(\widehat{S}_\varepsilon^r) \subset \Sigma_2$ is no longer a single curve, but consists of two curves that each spiral into the point $W^s(p) \cap \Sigma_2$, which is the light-blue dot located at the centre of Figure 3(c).

After the tangency the structure of S_ε^r changes dramatically. Figure 4(a) shows the same three-dimensional view shown in Figures 2(a) and 3(a), now for $\nu = 0.00712$ where the intersection between S_ε^r and $W^u(p)$ is transverse. Figure 4(b) shows their respective intersection sets in Σ_1 . The curve $\widehat{S}_\varepsilon^r$ is transverse to \widehat{W}_1 , so it intersects both $D(\pi_{12}^-)$ and $D(\pi_{13}^-)$, creating two intersection points $\hat{\zeta}_1$ (gold) and $\hat{\zeta}_2$ (brown) which correspond to the connecting canard orbits ζ_1 (gold) and ζ_2 (brown) that accumulate on p in backward time. The repelling slow manifold S_ε^r then intersects both Σ_2 and Σ_3 and it is divided into three pieces by ζ_1 and ζ_2 . The two segments of $\widehat{S}_\varepsilon^r$ that lie to the left of \widehat{W}_1 in panel (b) belong to $D(\pi_{12}^-)$ and correspond to orbits on S_ε^r that follow $W^u(p)$ from the ‘outside’; the corresponding pieces of S_ε^r are stretched, folded and pushed down by $W^s(p)$ as they approach p , intersecting Σ_2 in backward time. The

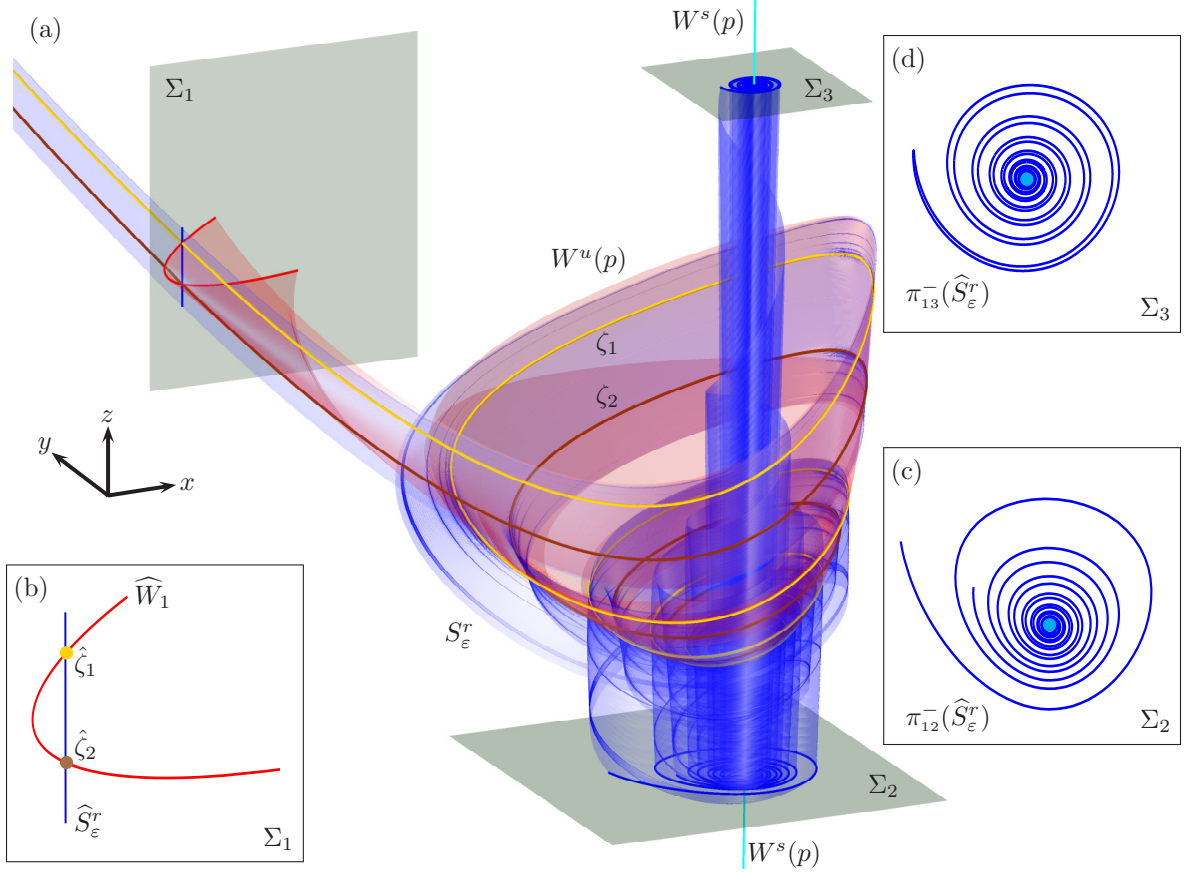


Figure 4: Intersection between S_ε^r (blue surface) and $W^u(p)$ (red surface) along two connecting canard orbits ζ_1 (gold curve) and ζ_2 (brown curve) of system (1) with $\nu = 0.00712$. Panel (a) shows the manifolds in (x, y, z) -space and panels (b) and (c) show their intersection curves with sections Σ_1 and Σ_2 , respectively. After a tangency, S_ε^r also intersects Σ_3 , which is shown in panel (d); compare with Figures 2 and 3.

intersection set $\pi_{12}^-(\widehat{S}_\varepsilon^r) \subset \Sigma_2$ shown in panel (c) then consists again of two curves that spiral around the point $W^s(p) \cap \Sigma_2$ and accumulate on it. The bounded segment of $\widehat{S}_\varepsilon^r$ that belongs to $D(\pi_{13}^-)$, on the other hand, lies to the right of \widehat{W}_1 in Σ_1 , and it corresponds to a connected family of trajectories on S_ε^r that follow $W^u(p)$ from the ‘inside’ and, as they approach p , spiral up around $W^s(p)$ to intersect Σ_3 in backward time. The intersection set $\pi_{13}^-(\widehat{S}_\varepsilon^r) \subset \Sigma_3$ shown in panel (d) is a single curve that connects at both ends with the point $W^s(p) \cap \Sigma_3$: it spirals out from $W^s(p) \cap \Sigma_3$ and back into it.

As soon as S_ε^r interacts with $W^u(p)$, the dynamics of S_ε^r around p changes. Figure 3(a) corresponds to the situation described in [7], where the tangency between S_ε^r and $W^u(p)$ was first detected with a shooting approach. Instead, we use here a boundary value problem setup, which provides accurate results in spite of the extreme sensitivity of system (1), allowing to track the intersection sets in Σ_1 as ν varies. More specifically, we employ a Lin’s method approach [32, 36, 39] to detect the connecting canard orbits as a codimension-zero transverse intersection between S_ε^r and $W^u(p)$ by considering their intersection sets $\widehat{S}_\varepsilon^r$ and \widehat{W}_1 in Σ_1 ; in this way, one obtains a well-defined test function for the intersections between $\widehat{S}_\varepsilon^r$ and \widehat{W}_1 . Once the intersection between S_ε^r and $W^u(p)$ is transverse, with our computational setup the detection of one connecting canard orbit implies the automatic detection of the other one. More importantly, our method also provides a way to detect the connecting canard orbit ζ^* together

with the tangency point $\hat{\zeta}^*$ in Σ_1 as a fold with respect to the parameter ν in the continuation of the connecting canard orbits; see the appendix for more details on how we find connecting canard orbits and detect the tangency point in Σ_1 . Overall, we are able to provide a complete understanding of the local picture by studying how $\widehat{S}_\varepsilon^r$ crosses the boundary between $D(\pi_{12}^-)$ and $D(\pi_{13}^-)$, and by extending S_ε^r past Σ_1 in backward time to Σ_2 and Σ_3 , respectively. We now focus on the global consequences of the first tangency between $W^u(p)$ and S_ε^r . To this end, we extend $W^u(p)$ past Σ_1 in forward time.

3.2 Global implications of the first tangency between S_ε^r and $W^u(p)$

The interaction between S_ε^r and $W^u(p)$ changes the shape of the repelling slow manifold and how it spirals around $W^s(p)$ when approaching p in backward time. As a consequence, the transition through the tangency changes the behaviour of orbits on $W^u(p)$ relative to S_ε^r as well. The tangency between S_ε^r and $W^u(p)$ occurs for $\nu = \nu^* \in (\nu_H^L, \nu_H^R)$, where system (1) has a globally attracting periodic orbit Γ_ν . This means that all orbits on $W^u(p)$ accumulate onto Γ_ν . Figure 5 shows a global view of the interaction between S_ε^r and $W^u(p)$ before, at and after the tangency in panels (a), (b) and (c), respectively. The parameter values are the same as for Figures 2, 3 and 4, respectively. Each panel uses the same view point and scaling, so that one can appreciate how $W^u(p)$ grows in size as it interacts with S_ε^r . We compute S_ε^r as a family of orbit segments with one end point on a line L^r that is transverse to the flow and lies on the repelling sheet S^r of the critical manifold S , close to the fold curve F^- ; the other end point either lies on Σ_2 , converges to p (connecting canard orbit) or lies on a local two-dimensional section parallel to and above Σ_3 . The repelling slow manifold S_ε^r , therefore, tracks the repelling sheet S^r of the critical manifold S all the way up to L^r .

Figure 5(a) shows the situation before the tangency. Here orbits on $W^u(p)$ spiral out from p and come close to S_ε^r before converging to Γ_ν (green curve). For this value of ν the two stable Floquet multipliers of Γ_ν are complex conjugate; therefore, $W^u(p)$ already scrolls around Γ_ν as it accumulates on the attracting periodic orbit. The repelling slow manifold S_ε^r has very little influence on the shape of $W^u(p)$. The moment of the tangency is shown in panel (b). The existence of the connecting canard orbit ζ^* (orange curve), implies that a trajectory on $W^u(p)$ tracks the middle branch of the critical manifold all the way up to the fold curve F^- . As a result, $W^u(p)$ has grown bigger and a substantial part of phase space is now pushed towards $W^s(p)$ and funneled back into a neighborhood of p ; compare panels (a) and (b) in Figure 5. Figure 5(c) shows a global picture of S_ε^r and $W^u(p)$ after the tangency, together with the periodic attractor Γ_ν (green curve). The unstable manifold $W^u(p)$ grows even larger in size as it intersects S_ε^r transversally; it crosses the sheets $S^{a,\pm}$ and S^r of S . Additionally, the unstable manifold $W^u(p)$ folds back over itself before accumulating onto Γ_ν due to a global return mechanism that bring orbits back to a neighborhood of p . This global return contains a slow passage tracking S^r , a jump along a fast fiber and a second slow passage tracking $S^{a,+}$ towards p . The connecting canard orbits ζ_1 and ζ_2 (gold and brown curves) perform the global return and are now situated well inside the range of $W^u(p)$.

4 Secondary tangencies of $W^u(p)$ with S_ε^r

Figure 5(c) shows that, for $\nu = 0.00712$, the unstable manifold $W^u(p)$ folds back over itself and returns to a neighborhood of p . The presence of a global return mechanism in the dynamics of system (1) implies that $\widehat{W}_1 \subset \Sigma_1$ intersects $D(\pi_{13}^+)$ and $D(\pi_{11}^+)$, which allows us to compute the intersection sets of $W^u(p)$ with Σ_3 and Σ_1 in forward time, respectively. As we have seen,

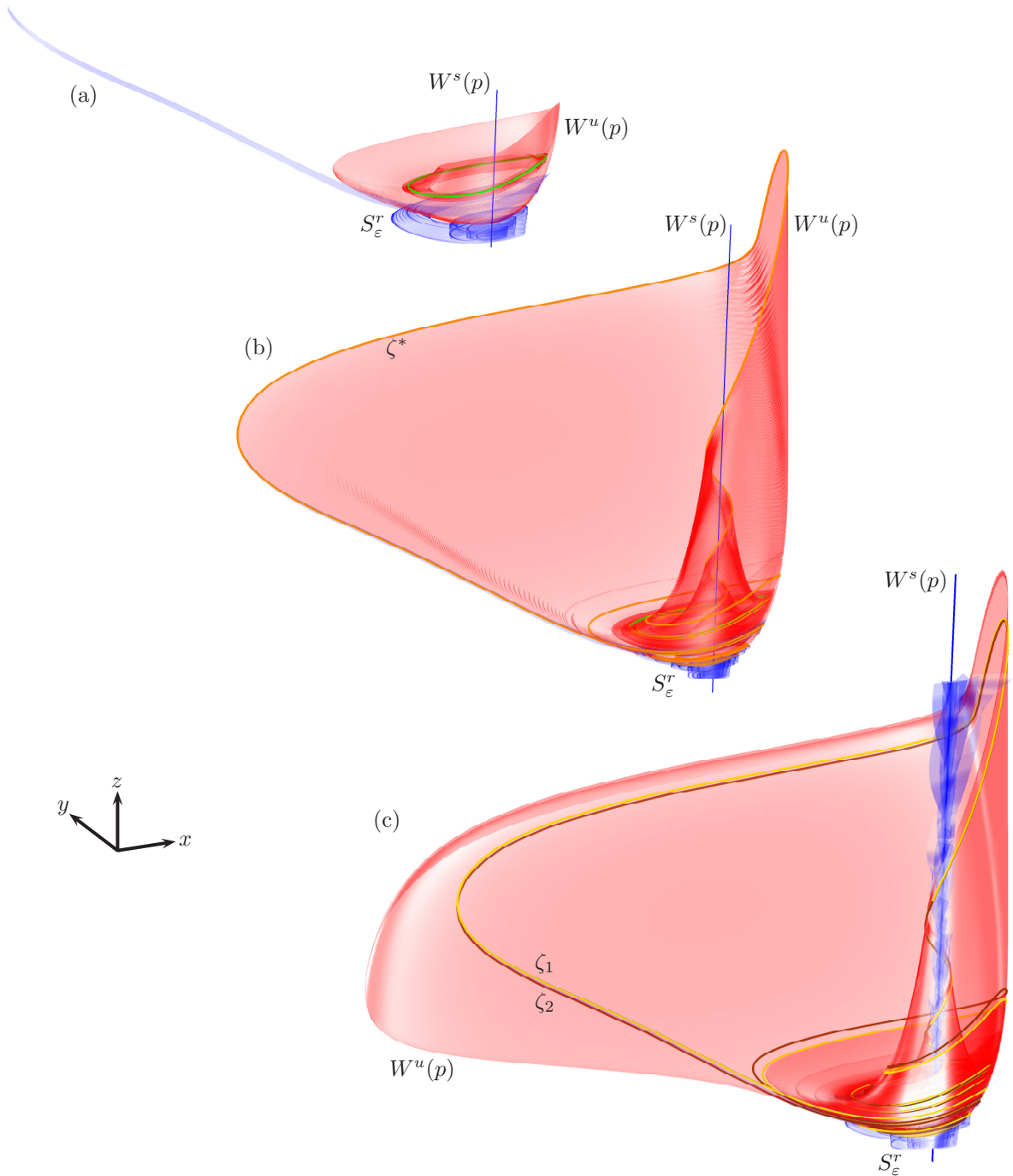


Figure 5: Global view of S_ε^r (blue surface), $W^u(p)$ (red surface) and Γ_ν (green curve) in (x, y, z) -space before, at and after the tangency in panels (a), (b) and (c), for the same values of ν that are used in Figures 2, 3 and 4, respectively. The connecting canard orbits ζ^* , ζ_1 and ζ_2 are the orange, gold and brown orbits, respectively.

the crossing of $\widehat{S}_\varepsilon^r$ through the boundary \widehat{W}_1 between the domains of definition of π_{12}^- and π_{13}^- results in a part of S_ε^r going up above p to Σ_3 in backward time. This indicates the existence of parameter regimes where there are families of orbits on $W^u(p)$ that interact with S_ε^r after the global return; we refer to these interactions as secondary interactions between $W^u(p)$ and S_ε^r . Figure 6 shows an extended part of $W^u(p)$ computed for $\nu = 0.00712$, seen from the same local view point as in Figure 4. Panel (a) illustrates the existence of a second intersection of

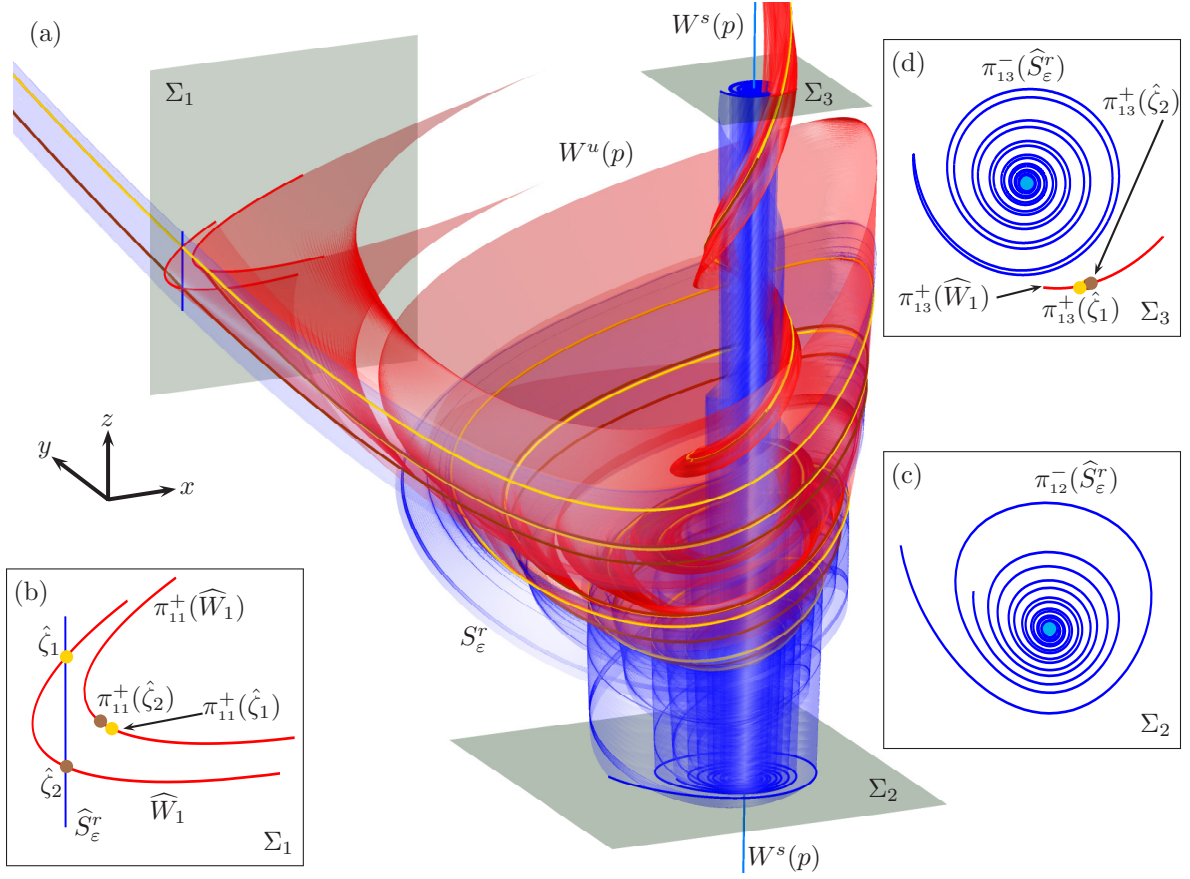


Figure 6: Secondary intersection of $W^u(p)$ with Σ_1 associated with the global return for $\nu = 0.00712$.

$W^u(p)$ with Σ_1 in (x, y, z) -space. The secondary intersection set shown in panel (b) corresponds to the image of \widehat{W}_1 under π_{11}^+ , which is also a parabola-shaped curve. The intersection sets $\pi_{12}^-(\widehat{S}_\varepsilon^r)$ of S_ε^r with Σ_2 in panel (c) and $\pi_{13}^-(\widehat{S}_\varepsilon^r)$ with Σ_3 in panel (d) are the same as in Figure 4, but the extended part of $W^u(p)$ gives rise to an intersection set $\pi_{13}^+(\widehat{W}_1) \subset \Sigma_3$ in panel (d) that is mapped by the flow to a secondary parabola $\pi_{11}^+(\widehat{W}_1)$ in Σ_1 . Note that $\pi_{11}^+(\widehat{W}_1) = \pi_{31}^+(\pi_{13}^+(\widehat{W}_1)) \subset \Sigma_1$ and $\pi_{13}^+(\widehat{W}_1) = \pi_{13}^+(\pi_{11}^+(\widehat{W}_1)) \subset \Sigma_3$; see panels (b) and (d). We get a good impression of the global nature of the return by considering the connecting canard orbits ζ_1 and ζ_2 . As shown in panels (b) and (d), ζ_1 and ζ_2 intersect Σ_1 at the points $\hat{\zeta}_1$ and $\hat{\zeta}_2$, respectively, and appear to come extremely close during the global return before they intersect Σ_3 at the points $\pi_{13}^+(\hat{\zeta}_1)$ and $\pi_{13}^+(\hat{\zeta}_2)$; they remain close as they intersect Σ_1 again at the corresponding points $\pi_{11}^+(\hat{\zeta}_1)$ and $\pi_{11}^+(\hat{\zeta}_2)$. In fact, the secondary local parabola $\pi_{11}^+(\widehat{W}_1) \subset \Sigma_1$ and the curve segment $\pi_{13}^+(\widehat{W}_1) \subset \Sigma_3$ shown in panels (b) and (d) of Figure 6, respectively, consist of two curve segments that lie extremely close to each other. For both connecting canard orbits ζ_1 and ζ_2 , there exist small curve segments I_{ζ_1} and I_{ζ_2} in $\widehat{W}_1 \subset \Sigma_1$ that contain $\hat{\zeta}_1$ and $\hat{\zeta}_2$, respectively, and correspond to orbits on $W^u(p)$ that exhibit a global return creating an intersection with Σ_3 and (locally) a secondary parabola in Σ_1 . In spite of being extremely close together, the two secondary parabolas must be different, because they are diffeomorphic images of two different disconnected segments under the flow.

Figure 7 shows the two families of orbits that create the two secondary parabolas for $\nu = 0.00712$; compare with Figure 6. Panel (a1) shows a three-dimensional view of the family of orbits on $W^u(p)$ whose first intersection with Σ_1 is I_{ζ_1} . This part of $W^u(p)$ looks like a thin

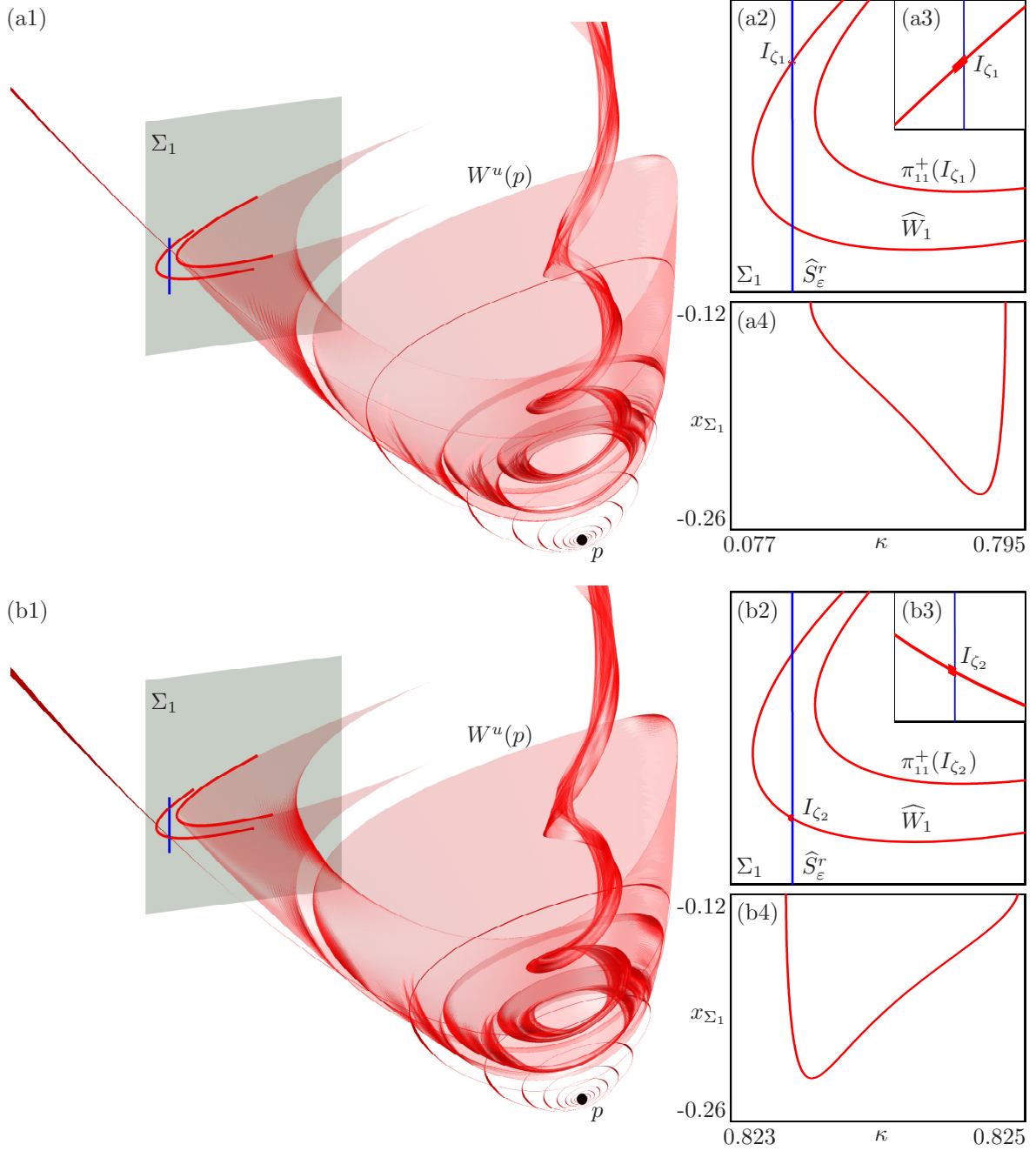


Figure 7: Secondary parabolas for $\nu = 0.00712$. Panels (a1) and (b1) show a three-dimensional view of parts of $W^u(p)$, as defined by segments I_{ζ_1} and I_{ζ_2} in Σ_1 , that produce secondary parabolas. Panels (a2) and (b2) show the intersection of $W^u(p)$ and S_ε^r with Σ_1 , with enlargements shown in panels (a3) and (b3), respectively. Panels (a4) and (b4) visualise the secondary parabolas by plotting their x -coordinates x_{Σ_1} in Σ_1 versus the parameter κ that identifies the corresponding orbits on $W^u(p)$ in the fundamental domain near p .

band as it spirals out from p , crosses Σ_1 , gets stretched in the global return before reaching Σ_3 ; it stretches even more when it spirals in and out of a neighborhood of p finally to intersect Σ_1 again to form a secondary parabola. Panel (a2) illustrates the two intersection sets \widehat{W}_1 and $\pi_{11}^+(I_{\zeta_1})$ of $W^u(p)$ with Σ_1 and their relative positions with respect to $\widehat{S}_\varepsilon^r$; an enlargement of the intersection between \widehat{W}_1 and $\widehat{S}_\varepsilon^r$ at $\hat{\zeta}_1$ is shown in the inset panel (a3). Panels (b1)–(b3) show the

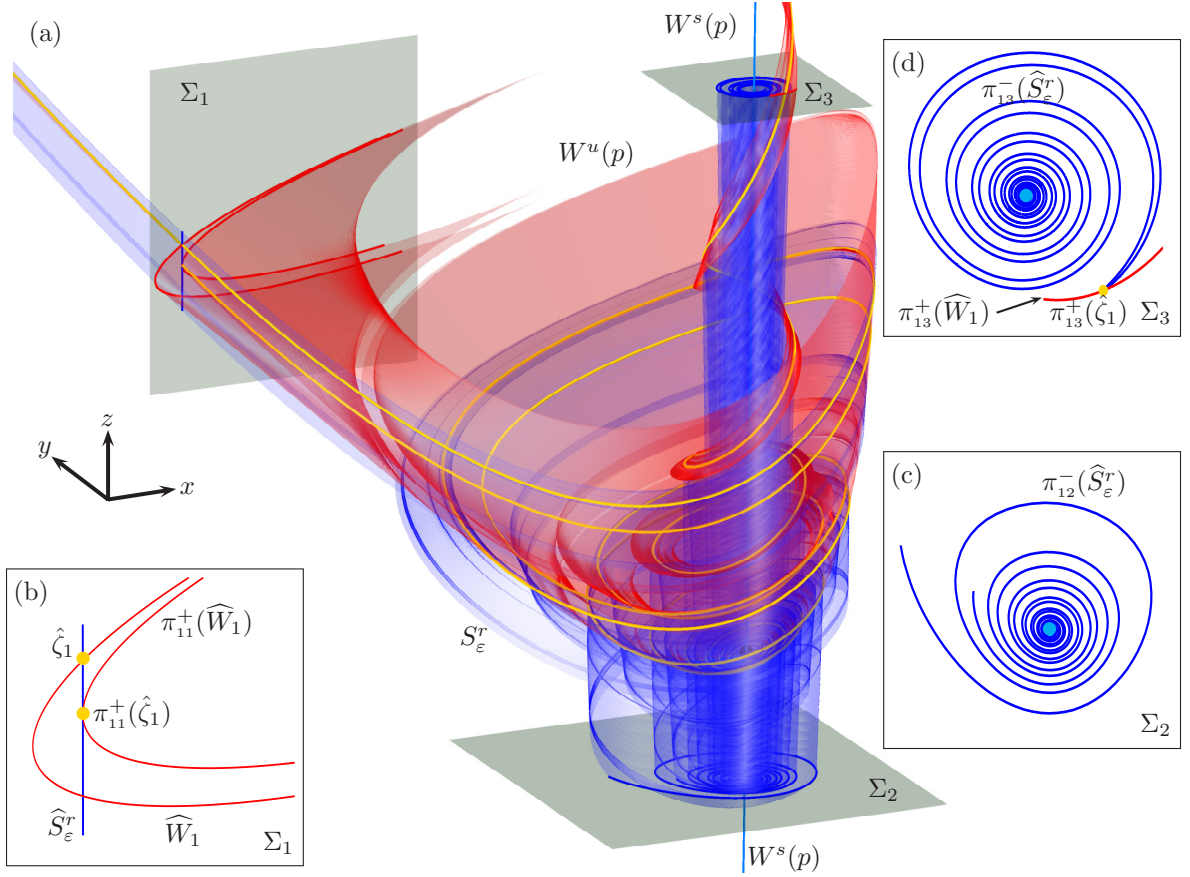


Figure 8: A secondary tangency between $W^u(p)$ and S_ε^r associated with the global return for $\nu = \nu^{**}$.

same visualisations for the different family of orbits on $W^u(p)$ associated with the segment I_{ζ_2} . Numerically, we compute $W^u(p)$ as a family of orbits segments that are solutions of a two-point boundary value problem, so that we have control of the two end points of each orbit segment. Particularly, for the parts of $W^u(p)$ shown in panels (a1) and (b1), one end point lies in what is known as a *fundamental domain* for $W^u(p)$, which is a finite line segment parameterised by a single parameter $\kappa \in [0, 1]$, such that points on it all correspond to different orbits of $W^u(p)$; see [30] for details. The other end point lies on Σ_1 and is controlled by boundary conditions, so that we can monitor their coordinates $(x_{\Sigma_1}, y_{\Sigma_1}, z_{\Sigma_1}) \in \Sigma_1$; note that $y_{\Sigma_1} = 0.03$. Figures 7(a4) and (b4) provide evidence that the second parabola that is visible in Figure 6(b) consists indeed of two curves. The graph of x_{Σ_1} as a function of the parameter κ for the families of orbits that create the parts of $W^u(p)$ are different, as is shown in the corresponding panels (a1) and (b1). The disjoint κ -intervals show that the parabolas are generated by two completely different families of orbit segments. Therefore, there are two distinct secondary parabolas.

Figure 8 illustrates that, when ν increases slightly, it generates a secondary quadratic tangency between S_ε^r and $W^u(p)$, that is, $\widehat{S}_\varepsilon^r$ is tangent to $\pi_{11}^+(\widehat{W}_1)$, which gives rise to a secondary connecting canard orbit ζ^{**} . This secondary tangency occurs at $\nu = \nu^{**} \approx 0.007155$. As before, panel (a) displays a local view of the surfaces in (x, y, z) -space, and panels (b)–(d) show the intersections sets in Σ_1 – Σ_3 , respectively. Since ζ^{**} intersects Σ_1 at a point $\hat{\zeta}^{**}$ on $\pi_{11}^+(\widehat{W}_1)$, it must also intersect Σ_1 at a point $\pi_{11}^-(\hat{\zeta}^{**})$ on \widehat{W}_1 . This pre-image of ζ^{**} must belong to either I_{ζ_1} or I_{ζ_2} . We found that I_{ζ_1} provides the orbit in $S_\varepsilon^r \cap W^u(p)$ that generates the first secondary tangency. Moreover, ζ^{**} lies extremely close to the (primary) connecting canard orbit ζ_1 . Fig-

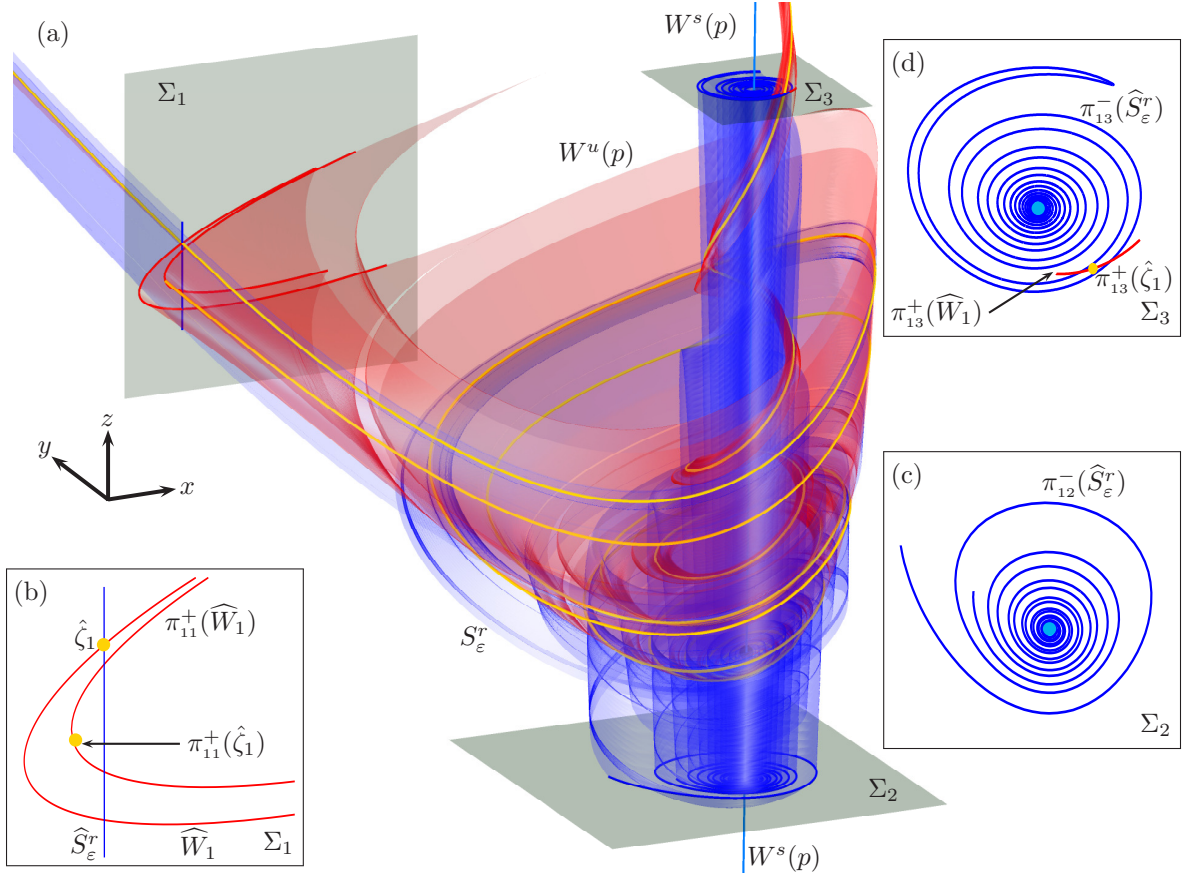


Figure 9: A transverse secondary intersection between $W^u(p)$ and S_ε^r associated with the global return for $\nu = 0.00722$.

Figure 8 shows the manifolds for $\nu = \nu^{**}$ together with the (primary) connecting canard ζ_1 up to its second intersection $\pi_{11}^+(\hat{\zeta}_1)$ with Σ_1 . The point $\pi_{11}^+(\hat{\zeta}_1) \in \Sigma_1$ lies extremely close to the tangency point $\hat{\zeta}^{**}$ (not shown) of $\pi_{11}^+(\widehat{W}_1)$ with $\widehat{S}_\varepsilon^r$ in Σ_1 . Furthermore, $\pi_{13}^+(\widehat{W}_1)$ is also tangent to $\pi_{13}^-(\widehat{S}_\varepsilon^r)$ in Σ_3 and the intersection point $\pi_{13}^+(\hat{\zeta}_1)$ of ζ_1 with Σ_3 is also extremely close to the tangency point $\pi_{13}^-(\hat{\zeta}^{**})$ between $\pi_{13}^-(\widehat{S}_\varepsilon^r)$ and $\pi_{13}^+(\widehat{W}_1)$ in Σ_3 ; compare panels (b) and (d).

Figure 9 shows a transverse secondary intersection of $W^u(p)$ with S_ε^r for $\nu = 0.00722$. There exists a part of $W^u(p)$ that crosses Σ_1 , is reinjected to a neighborhood of p by spiralling around $W^s(p)$, leaves the neighborhood of p and crosses Σ_1 again, where it intersects $\widehat{S}_\varepsilon^r$ transversally. This part of $W^u(p)$ contains ζ_1 , whose second intersection $\pi_{11}^+(\hat{\zeta}_1)$ with Σ_1 lies to the left of $\widehat{S}_\varepsilon^r$; see panel (b). Hence, the intersection of $\pi_{13}^+(\widehat{W}_1)$ and $\pi_{13}^-(\widehat{S}_\varepsilon^r)$ in Σ_3 is now transverse as well, and the connecting canard orbit ζ_1 intersects Σ_3 at the point $\pi_{13}^+(\hat{\zeta}_1)$ located in the interior of the open region bounded by $\pi_{13}^-(\widehat{S}_\varepsilon^r) \subset \Sigma_3$; see panel (d). Note that Γ_ν is still the boundary of $W^u(p)$, but some orbits of $W^u(p)$ take much longer to converge to Γ_ν because of the multiple returns to a neighborhood of p and, thus, to Σ_1 .

Since $\pi_{11}^+(\widehat{W}_1)$ consists of two parabolas locally in Σ_1 , the transition illustrated in Figures 6, 8 and 9 must include another secondary tangency between S_ε^r and $W^u(p)$, namely, one involving the parabola in $\pi_{11}^+(I_{\zeta_2})$ generated by the segment $I_{\zeta_2} \subset \widehat{W}_1$. This tangency follows immediately after the first one at a value of ν that is only slightly larger than ν^{**} . The exact parameter value for that tangency is numerically indistinguishable from ν^{**} , even though the corresponding orbit segments can be distinguished clearly.

The transverse secondary intersection between $W^u(p)$ and S_ε^r implies the existence of secondary connecting canard orbits, which is very important for the organisation of recurrent dynamics in system (1). After a secondary tangency occurs, the unstable manifold $W^u(p)$ has parts that perform several large excursions since images of \widehat{W}_1 under π_{11}^+ intersect $D(\pi_{11}^+)$ near $\widehat{S}_\varepsilon^r$. Additionally, $W^u(p)$ folds back over itself several times and its geometry becomes far more complicated. In the same way as for the study of the local dynamics described in Section 3.1, our boundary problem setup allows us to compute secondary connecting canard orbits and detect secondary tangencies between $W^u(p)$ and S_ε^r in Σ_1 . We have considered a local segment of the set \widehat{W}_1 of first intersection of $W^u(p)$ with Σ_1 . Now we describe global consequences of the existence of secondary connecting canard orbits and where they come from in \widehat{W}_1 . To this end, we consider how the maps π_{11}^+ , π_{11}^- act on the full intersection set \widehat{W}_1 .

4.1 Global view of sections Σ_1 and Σ_3

In order to understand the global nature of the interaction between $W^u(p)$ and S_ε^r , we compute the entire first intersection sets \widehat{W}_1 and $\pi_{13}^+(\widehat{W}_1)$ of $W^u(p)$ with Σ_1 and Σ_3 past the secondary tangency, namely again for $\nu = 0.00722$. Figure 10 shows $\widehat{W}_1 \subset \Sigma_1$ and $\pi_{13}^+(\widehat{W}_1) \subset \Sigma_3$ in panels (a) and (b), respectively. Panel (a1) shows that $\widehat{W}_1 \subset \Sigma_1$ (red) is a simple closed curve. For this parameter value $\widehat{W}_1 \subset D(\pi_{13}^+)$; hence, \widehat{W}_1 is mapped diffeomorphically onto Σ_3 as the simple closed curve $\pi_{13}^+(\widehat{W}_1)$ shown in panel (b1). This curve spirals around $\pi_{13}^-(\widehat{S}_\varepsilon^r)$ while it is compressed strongly, so that it looks like a single curve. Notice that $\pi_{13}^+(\widehat{W}_1)$ intersects $\pi_{13}^-(\widehat{S}_\varepsilon^r)$ in Σ_3 , thus creating secondary connecting canard orbits. As Figure 10(a1) shows, $\pi_{11}^+(\widehat{W}_1)$ lies inside the region bounded by the closed curve \widehat{W}_1 . Notice the extreme expansion in the fast direction x and the compression in the slow direction z in forward time. It is hard to see from the global view in panel (a1), but the curve $\pi_{11}^+(\widehat{W}_1)$ is also a simple closed curve.

From Figure 9 in Section 4 we already know that the secondary intersection of $W^u(p)$ with Σ_1 is such that it generates further intersections with S_ε^r . This is illustrated further in the enlargement panels (a2) and (a3) of Figure 10. Recall from Section 4 that $\pi_{11}^+(\widehat{W}_1)$ contains two local parabolas in Σ_1 . Hence, the point $\hat{\zeta} \in \pi_{11}^+(\widehat{W}_1) \cap \widehat{S}_\varepsilon^r$ shown in panel (a2), which corresponds to a secondary connecting canard orbit ζ , is one of the four intersection points between $\pi_{11}^+(\widehat{W}_1)$ and $\widehat{S}_\varepsilon^r$. Panel (a3) provides an even closer enlargement around $\hat{\zeta}$. Since $\hat{\zeta} \in \pi_{11}^+(\widehat{W}_1)$, this point comes back to Σ_1 in backward time at the point $\pi_{11}^-(\hat{\zeta}) \in \widehat{W}_1$. The point $\hat{\zeta}$ also lies on $\widehat{S}_\varepsilon^r$, so there exist a segment of $\widehat{S}_\varepsilon^r$ that returns in backward time to Σ_1 . Despite the strong expansion in backward time and the extreme sensitivity of system (1), we manage to compute (a part of) the return $\pi_{11}^-(\widehat{S}_\varepsilon^r)$ of $\widehat{S}_\varepsilon^r$ to Σ_1 . Figure 10(a2) shows that $\pi_{11}^-(\widehat{S}_\varepsilon^r)$ lies extremely close to $\widehat{S}_\varepsilon^r$ in Σ_1 and intersects \widehat{W}_1 . More importantly, $\pi_{11}^-(\hat{\zeta})$ is one of the intersection points; it is expected that there are four of them. The recurrence to Σ_1 can also be understood in Σ_3 , where $W^u(p)$ and S_ε^r already interact. Figure 10(b2) shows an enlargement around the point $\pi_{13}^-(\hat{\zeta}) \in \pi_{11}^+(\widehat{W}_1) \cap \pi_{13}^-(\widehat{S}_\varepsilon^r)$, illustrating that the intersection set consists of four points.

Since $\pi_{11}^-(\widehat{S}_\varepsilon^r)$ lies so close to $\widehat{S}_\varepsilon^r$, we found that $\pi_{11}^+(\widehat{W}_1)$ intersects not only $\widehat{S}_\varepsilon^r$, but also $\pi_{11}^-(\widehat{S}_\varepsilon^r)$. One such point is labeled $\pi_{11}^-(\hat{\mu})$ in the further enlargement Figure 10(a2) around the intersection between \widehat{W}_1 and $\widehat{S}_\varepsilon^r$ in Σ_1 , which includes $\pi_{11}^+(\widehat{W}_1)$ as well as $\pi_{11}^-(\widehat{S}_\varepsilon^r)$. By the same argument as for $\hat{\zeta} \in \pi_{11}^+(\widehat{W}_1) \cap \widehat{S}_\varepsilon^r$, the point $\pi_{11}^-(\hat{\mu})$ in panel (a2) corresponds to an intersection between $\pi_{11}^+(\widehat{W}_1)$ and $\pi_{11}^-(\widehat{S}_\varepsilon^r)$ in Σ_1 , so there must exist a backward image $\pi_{11}^-(\pi_{11}^-(\widehat{S}_\varepsilon^r))$ of $\pi_{11}^-(\widehat{S}_\varepsilon^r)$ in Σ_1 and a point $\pi_{11}^-(\pi_{11}^-(\hat{\mu}))$ in Σ_1 that lies on the intersection of $\pi_{11}^-(\pi_{11}^-(\widehat{S}_\varepsilon^r))$ with

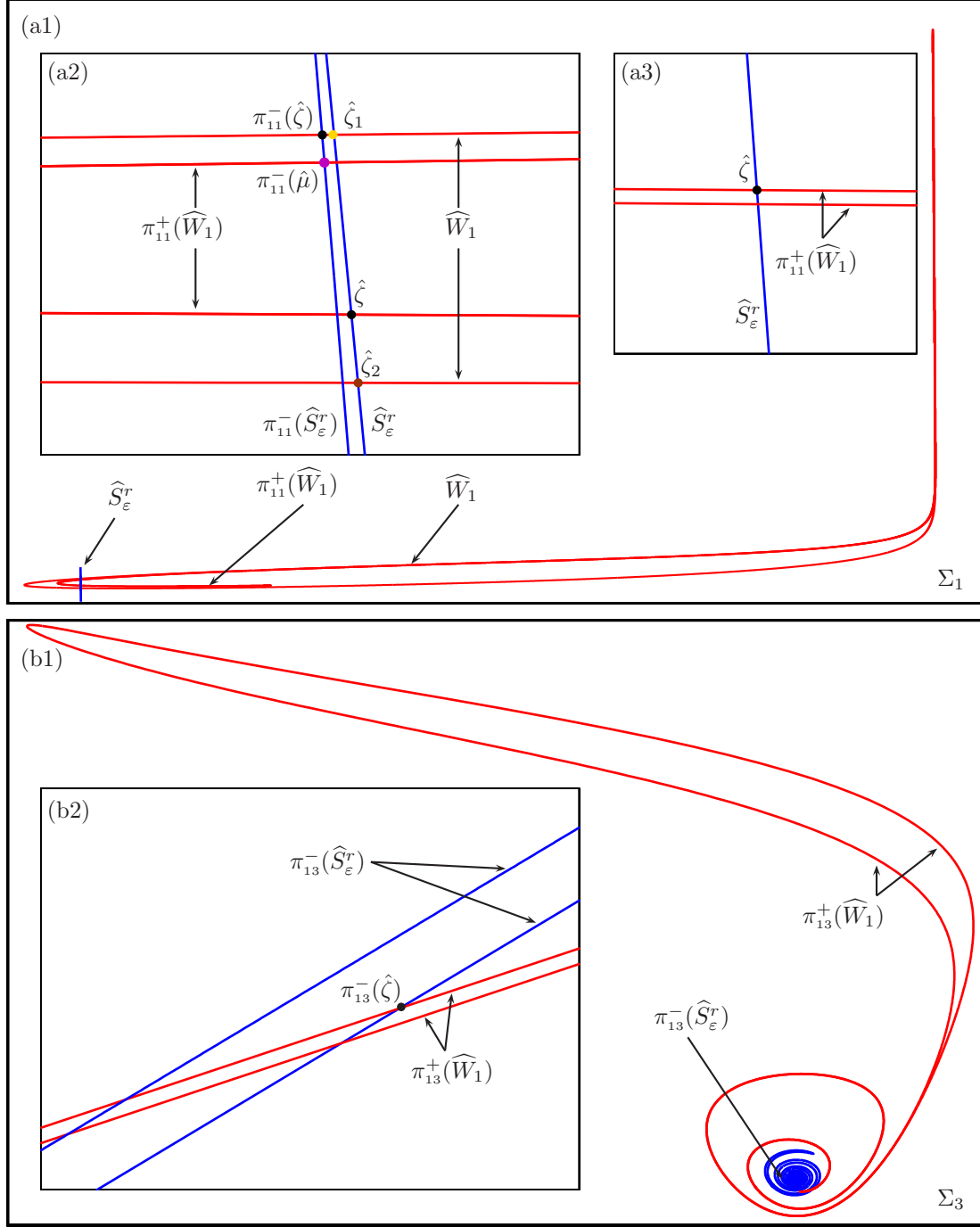


Figure 10: Global views of sections Σ_1 and Σ_3 , respectively. Panel (a1) shows the sets \widehat{W}_1 , $\pi_{11}^+(\widehat{W}_1)$ and $\widehat{S}_\varepsilon^r$, while panel (b1) shows the sets $\pi_{13}^+(\widehat{W}_1)$ and $\pi_{13}^-(\widehat{S}_\varepsilon^r)$. Panels (a2), (a3) and (b2) are enlargements near the intersections between the sets in the corresponding sections.

\widehat{W}_1 . In addition, there must exist a forward image of $\pi_{11}^-(\hat{\mu})$ that lies on $\widehat{S}_\varepsilon^r$, which implies that there must exist a third intersection $\pi_{11}^+(\pi_{11}^+(\widehat{W}_1))$ of $W^u(p)$ with Σ_1 .

Overall, Figure 10 indicates that a transverse secondary intersection between $W^u(p)$ and S_ε^r has additional global consequences. The domains of definition of π_{11}^+ , π_{13}^+ , π_{11}^- and π_{13}^- interact in a complicated way, and both $\widehat{S}_\varepsilon^r$ and \widehat{W}_1 intersect some of these sets. Every time a forward image of \widehat{W}_1 under π_{11}^+ intersects $\widehat{S}_\varepsilon^r$ in Σ_1 , there must exist a next return of $W^u(p)$ to Σ_1 . Similarly, every time a backward image of $\widehat{S}_\varepsilon^r$ under π_{11}^- intersects a forward image of \widehat{W}_1 under

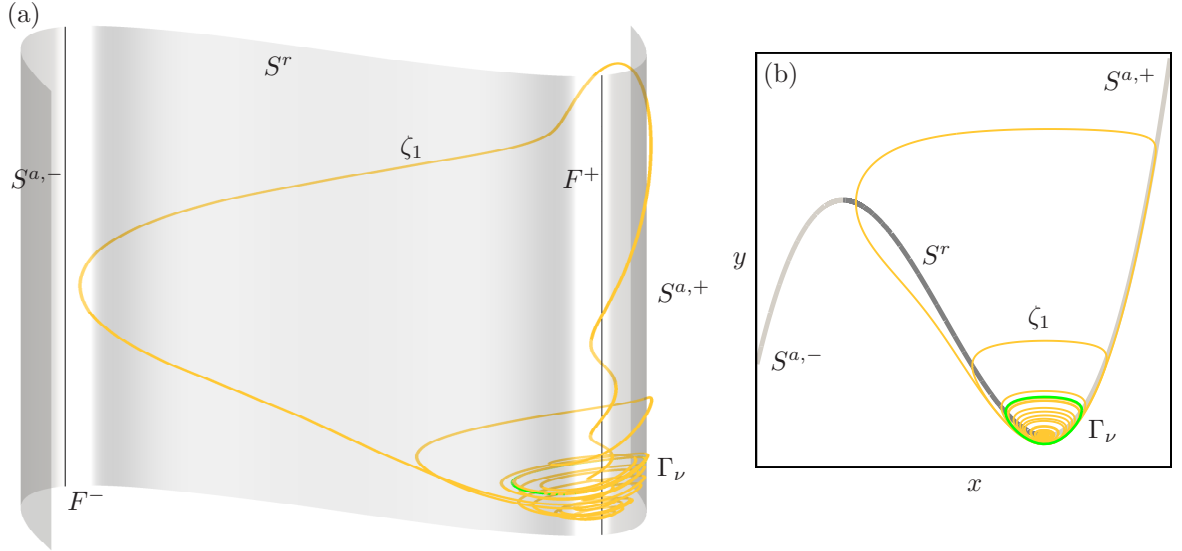


Figure 11: The connecting canard orbit ζ_1 (gold) for $\nu = 0.00722$, which converges to the periodic orbit Γ_ν (green). Panel (a) shows ζ_1 and the critical manifold of system (1) in (x, y, z) -space and panel (b) is the projection onto the (x, y) -plane.

π_{11}^+ in Σ_1 , there must exist a next return of S_ε^r to Σ_1 in backward time. Hence, the interaction between $W^u(p)$ and S_ε^r produces some kind of tangle in Σ_1 in the shape of an incomplete horseshoe composed of finitely many curves. Even though we only have the beginning of a horseshoe structure, we expect the existence of periodic orbits different from Γ_ν in system (1) involving both slow and fast motion.

5 Global MMO periodic orbits

It is known that the existence of a full horseshoe structure in a dynamical system implies the existence of chaos and countably many periodic orbits [4, 40, 45]. We expect that the finite horseshoe-like structure found in system (1) implies the existence of periodic orbits as well. Such periodic orbits will exhibit periodic motion with both LAOs and SAOs and, hence, they are examples of MMOs. The simplest such MMO periodic orbit would have a similar structure (of global return) as the connecting canard orbits ζ_1 and ζ_2 , which are maximal canards since they track S^r all the way up to the fold curve F^- . Figure 11 illustrates how ζ_1 lies relative to the critical manifold S , which is shown globally in (x, y, z) -space in panel (a) and in projection onto the (x, y) -plane in panel (b). Note that ζ_1 has seven SAOs and one LAO before settling down on Γ_ν . More specifically, the SAOs are due to spiraling in a neighborhood of the saddle focus p and the LAO corresponds to a global return after a slow epoch of tracking the repelling sheet S^r and the attracting sheet $S^{a,+}$ of S , with a jump between S^r and $S^{a,+}$ along a fast fiber. Therefore, we expect to find MMO periodic orbits nearby, with seven SAOs and one LAOs, that is, with signature 1^7 .

In order to find such an MMO periodic orbit, we truncate the connecting canard orbit associated to the point $\hat{\zeta}$ in Figure 10 to a finite orbit segment of signature 1^7 , whose end points are both in Σ_1 . The distance between these end points is very small, and this orbit segment is used as the initial guess for the solution of the two-point boundary value problem defining a periodic orbit, that is, where the two end points in Σ_1 are the same. The closing

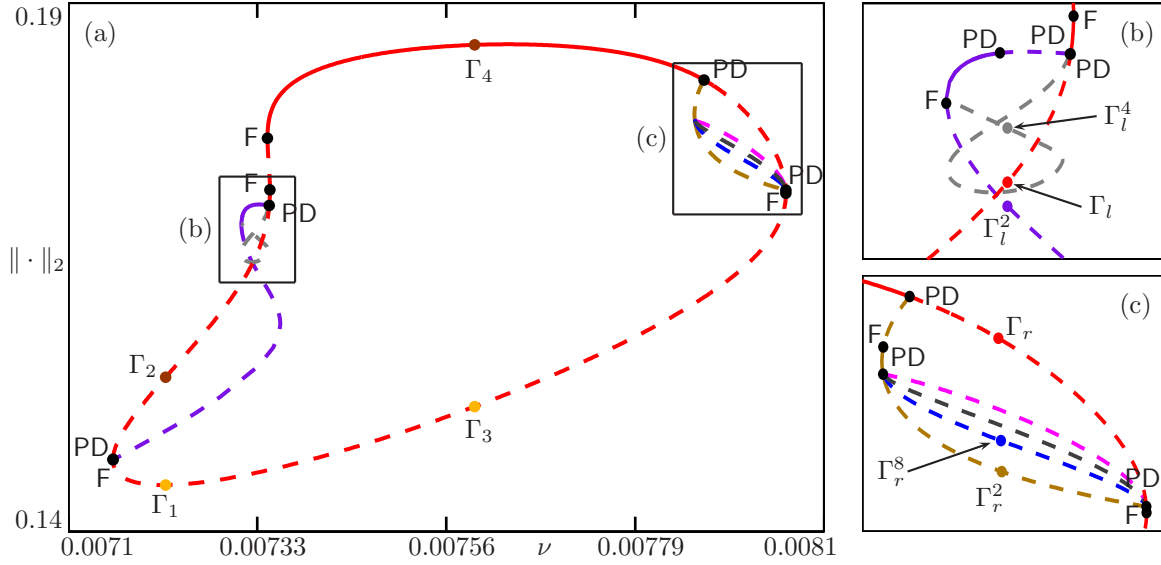


Figure 12: An isola of MMO periodic orbits with signature 1^7 in panel (a). The periodic orbits are stable along the solid branch and of saddle type otherwise. The dots in panel (a) indicate the position of the periodic orbits Γ_1 – Γ_4 shown in Figure 13. Enlargements of the boxes around period-doubling bifurcations are shown in panels (b) and (c). The dots in panels (b) and (c) similarly indicate the position of the periodic orbits Γ_l , Γ_l^2 , Γ_l^4 , Γ_r , Γ_r^2 and Γ_r^8 shown in Figure 14(a).

lemma [41, 42] implies that such a guess should be expected to converge to a nearby periodic orbit when the parameter ν is allowed to change. This is indeed the case and the MMO periodic orbit Γ_1 that is found can be continued in parameters as usual. It turns out that Γ_1 lies on an isola of MMO periodic orbits with signature 1^7 .

Figure 12 shows this isola and associated further bifurcations. Panel (a) shows solution branches in terms of the (AUTO) L_2 -norm $\|\cdot\|_2$ of the MMO periodic orbits in dependence on the parameter ν . The 1^7 isola (red curve) is created at a fold bifurcation of MMO periodic orbits at a value of ν that lies extremely close to, but just past $\nu^{**} \approx 0.007155$ where there is a secondary tangency between $W^u(p)$ and S_ε^r . The MMO periodic orbits exist until $\nu \approx 0.007983$, where another fold bifurcation of periodic orbits occurs. The lower branch of the isola is unstable, while the upper branch changes stability several times. Importantly, the MMO periodic orbit 1^7 is stable along a considerable part of the upper branch. There exists an interval $I_{bs} \subset (0.00734524, 0.00788233)$ of bistability, where the periodic orbit Γ_ν born after the supercritical singular Hopf bifurcation at $\nu = \nu_{\text{H}}^L$ is still stable; see already Figure 13. There are more small intervals of bistability, most of them too small to be visible in Figure 12(a); for example, near the fold bifurcation that forms the left boundary of the large interval of stable MMO periodic orbits.

Some of the changes of stability of the upper branch of the isola involve period-doubling bifurcations. Panels (b) and (c) of Figure 12 show enlargements as indicated by the boxes in panel (a). Subsequent period-doubling bifurcations create branches of period-doubled periodic orbits, which are mostly unstable. The period-doubled periodic orbits are MMOs as well, and some of them are shown in Figure 14.

Figure 13 shows the MMO periodic orbits Γ_1 – Γ_4 , represented by dots on the isola in Figure 12(a), together with Γ_ν . Panel (a) shows in (x, y, z) -space the saddle MMO periodic orbits Γ_1 and Γ_2 with the stable periodic orbit Γ_ν for $\nu = 0.00722$. Note that, during the global return,

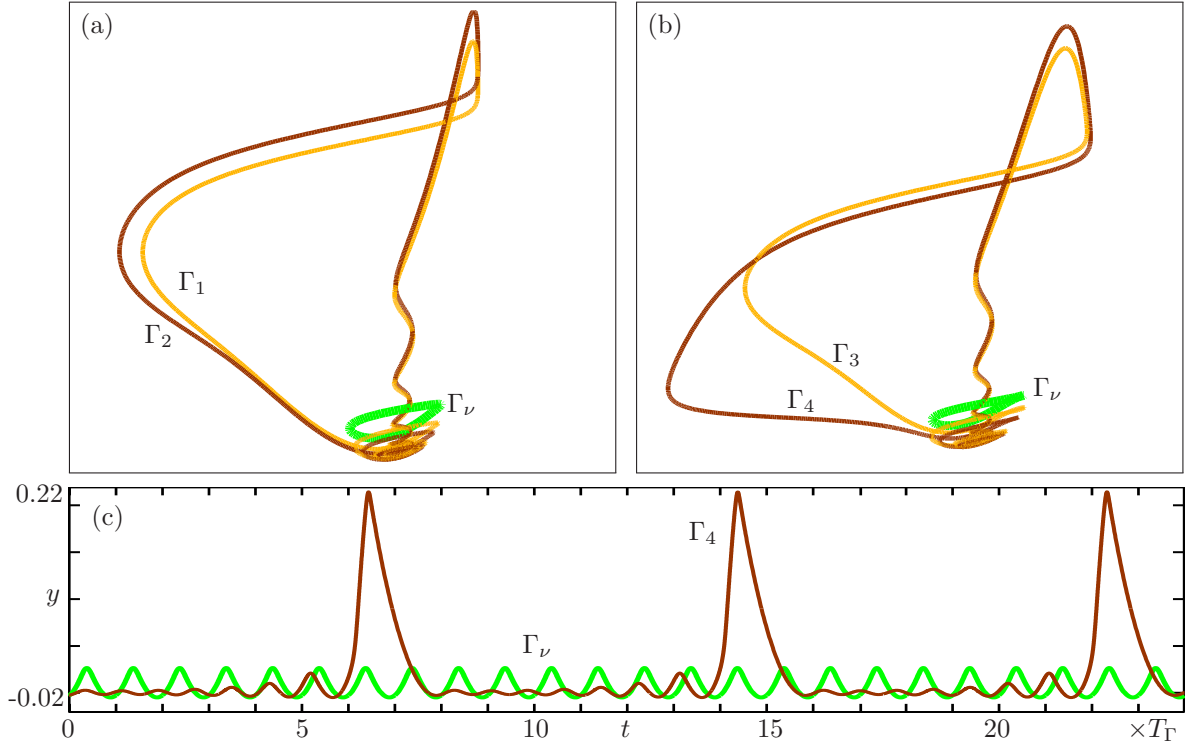


Figure 13: MMO periodic orbits Γ_1 – Γ_4 , which are linked with Γ_ν . Panel (a) shows Γ_1 , Γ_2 and Γ_ν for $\nu = 0.00722$, and panel (b) shows Γ_3 , Γ_4 and Γ_ν for $\nu = 0.0076$. Panel (c) shows the time series of the y -coordinate along the stable periodic orbits Γ_4 and Γ_ν from panel (b).

Γ_1 and Γ_2 are very close to the connecting canard orbits ζ_1 and ζ_2 , respectively, which is why Γ_1 and Γ_2 are represented by the same colour as ζ_1 and ζ_2 . Moreover, Γ_1 and Γ_2 are both (topologically) linked with Γ_ν . Similarly, panel (b) shows Γ_3 and Γ_4 , which are the continuations of Γ_1 and Γ_2 , respectively, to $\nu = 0.0076$; the MMO periodic orbits Γ_3 and Γ_4 are also linked with Γ_ν and Γ_4 is stable. The time series of the y -coordinates of the stable periodic orbits Γ_4 and Γ_ν are shown in Figure 13(c). They are displayed from $t = 0$ to $t = 24 \times T_{\Gamma_\nu} \approx 3 \times T_{\Gamma_4}$, where $T_{\Gamma_\nu} \approx 81.297$ is the period of Γ_ν and $T_{\Gamma_4} \approx 645.893$ is the period of Γ_4 ; this illustrates how the SAOs arise from spiralling of Γ_4 away from p .

Figure 14 shows some of the period-doubled MMO periodic orbits that lie on the branches of period-doubled solutions arising from the isola. Panels (a1) and (a2) show for $\nu = 0.00733$ the periodic orbits Γ_l^2 (purple) and Γ_l^4 (gray), respectively, each with Γ_l (red) and Γ_ν ; these periodic orbits are indicated by dots in Figure 12(b) and their colour matches that of the corresponding branch of period-doubling. The MMO periodic orbit Γ_l lies on the isola, while Γ_l^2 and Γ_l^4 lie on the primary and secondary branches of period-doubled solutions, respectively. Panels (b1) and (b2) of Figure 14 show for $\nu = 0.00792$ the orbits Γ_r^2 (olive) and Γ_r^8 (blue), each with Γ_r (red) and Γ_ν ; these periodic orbits are indicated by dots in Figure 12(c), where it can be seen that the MMO periodic orbit Γ_r lies on the isola, while Γ_r^2 and Γ_r^8 lie on the first and third branch of period-doubled solutions, respectively. Even though the periodic orbits on the different secondary branches of period-doubled solutions perform more global returns before closing up, each LAO is still followed by seven SAOs. Hence, the period-doubled MMO periodic orbits all have signature 1^7 as well; moreover, they are all linked with Γ_ν .

We found a complicated structure of 1^7 MMO periodic orbits lying on an isola, where the periodic orbits undergo further bifurcations. Figure 12(c) suggests an accumulation of unstable branches of high-order period doublings. One might suspect that this could lead to a

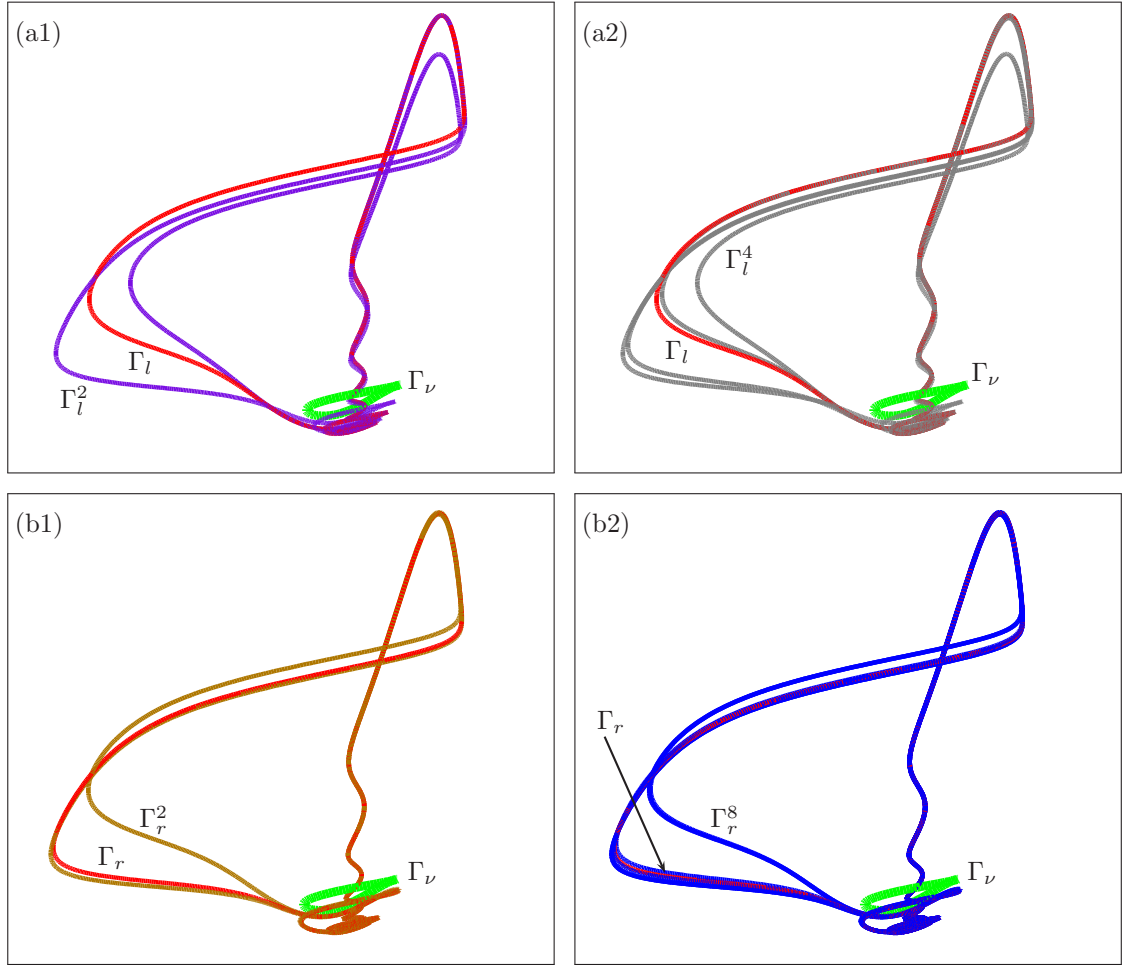


Figure 14: Period-doubled MMO periodic orbits. Row (a) shows the periodic orbits Γ_ν , Γ_l , Γ_l^2 and Γ_l^4 for $\nu = 0.00733$ from Figure 12(b), and row (b) shows the periodic orbits Γ_ν , Γ_r , Γ_r^2 and Γ_r^8 for $\nu = 0.00792$ from Figure 12(c).

period-doubling route to chaos and the existence of a chaotic attractor. However, we have not found numerical evidence for this. Rather, the structure appears to be of saddle type. More specifically, our investigation showed that some orbits with initial condition close to one of the saddle period-doubled MMO periodic orbits wander around the coexisting saddle periodic orbits for a long time before they accumulate on the attractor Γ_ν . These ‘wandering’ orbits feature long transients of 1^7 MMO signature with short segments of different MMO signatures.

Figure 15(a) shows an example of an orbit for $\nu = 0.00787125$ that accumulates on Γ_ν after a long transient. The time series of its y -coordinate up to $t = 45000$ shows that it is characterised by having MMO signature 1^7 for a long time before the orbit settles down on Γ_ν . However, the highlighted segment at the beginning of the time series has MMO signature $1^7 1^5$; an enlargement is shown in Figure 15(b). The two end points of the orbit segment, chosen to lie in Σ_1 , are extremely close to each other. Hence, with the same procedure as before the gap between the end points in Σ_1 can be closed in a solution step of the respective boundary value problem. This yields an MMO periodic orbit with signature $1^7 1^5$; the time series of its y -coordinate is shown in Figure 15(c).

When it is continued, the MMO periodic orbit with signature $1^7 1^5$ forms an isola as well. Figure 16(a) shows the $1^7 1^5$ isola (dark red) and the 1^7 isola (gray) from Figure 12(a) over the range $\nu \in (0.0071, 0.0081)$. For $\nu = 0.00787125$, there are four coexisting saddle MMO periodic

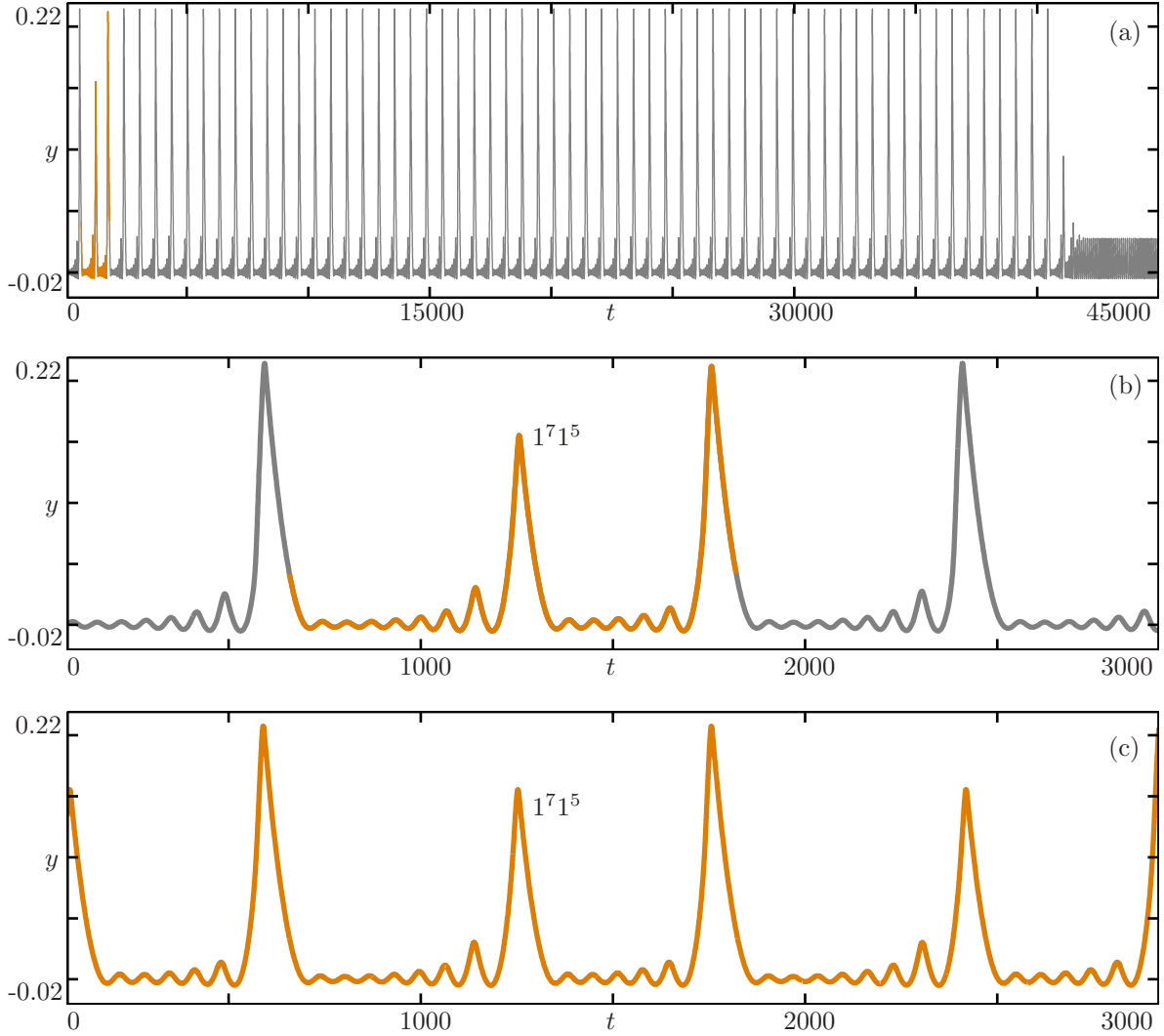


Figure 15: Panel (a) shows the time series of the y -coordinate of an orbit for $\nu = 0.00787125$ that wanders around the period-doubled saddle MMO periodic orbits before settling down on Γ_ν . Panel (b) is an enlargement near the highlighted orbit segment with MMO signature $1^7 1^5$. Panel (c) shows the time series of the nearby MMO periodic orbit with signature $1^7 1^5$.

orbits $\tilde{\Gamma}_1$ - $\tilde{\Gamma}_4$ on the $1^7 1^5$ isola, marked by dots. Panel (b) shows $\tilde{\Gamma}_1$ (blue), with $\tilde{\Gamma}_2$ (black) and Γ_ν (green), panel (c) shows $\tilde{\Gamma}_3$ (magenta), with $\tilde{\Gamma}_1$ and Γ_ν and panel (d) shows $\tilde{\Gamma}_4$ (golden), with $\tilde{\Gamma}_1$ and Γ_ν . All the MMO periodic orbits along the $1^7 1^5$ isola are of saddle type and linked with Γ_ν .

Overall, the interaction between $W^u(p)$ and S_ε^r generates complicated dynamics in system (1), which is organised by returns of $W^u(p)$ and S_ε^r to Σ_1 . We suspect that there are only finitely many such returns to Σ_1 , yet this configuration still gives a considerable amount of recurrent dynamics. We found MMO periodic orbits lying on isolas, which are generically quite hard to find. This demonstrates the strength and versatility of our boundary value problem setup for detecting and continuing special orbits. In particular, it copes well with the sensitivity of slow-fast systems such as system (1). All the MMO periodic orbits of an isola have the same MMO signature and are linked with Γ_ν . We conjecture that these isolas, and possibly other ones are generated by the saddle structure we found in system (1), in the parameter range where branches of period-doubled solutions accumulate.

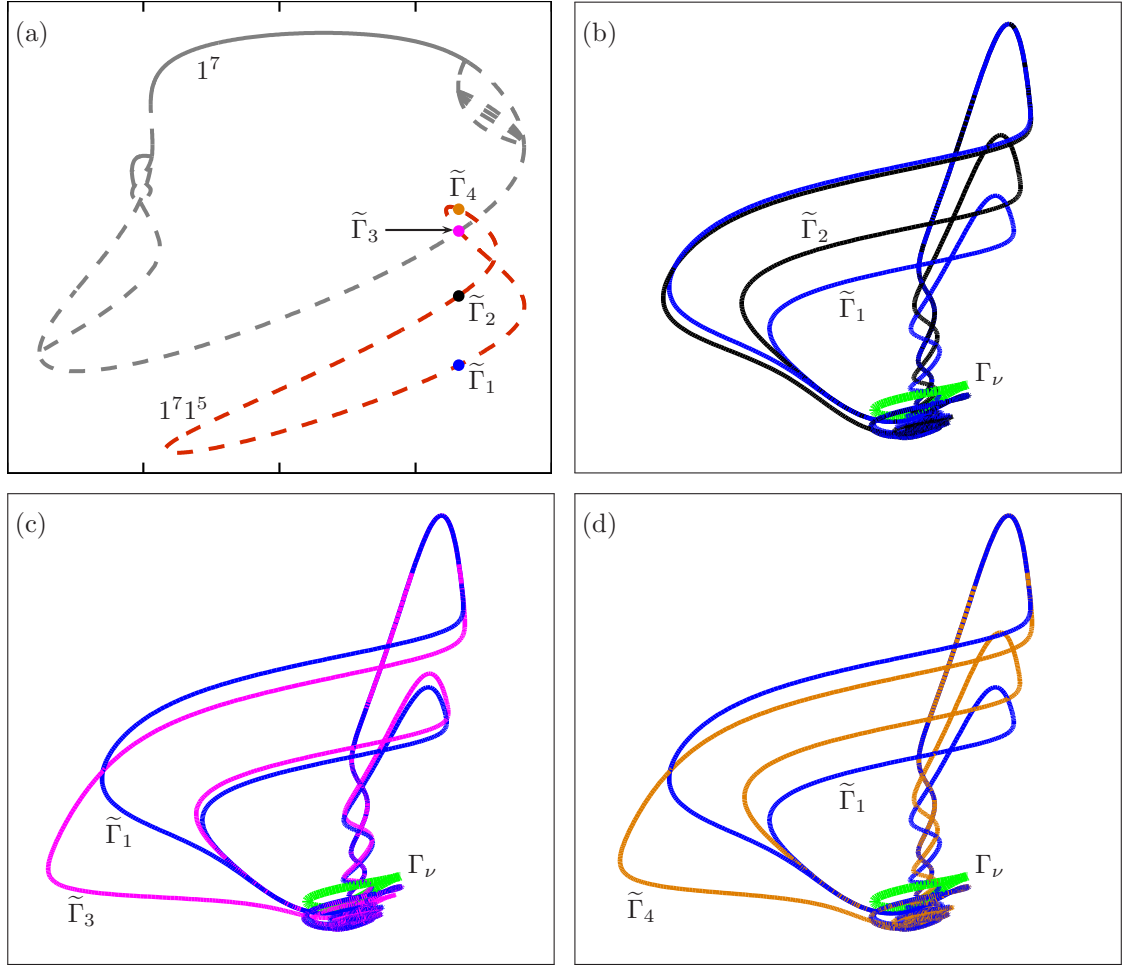


Figure 16: Illustration of MMO periodic orbits of signature $1^7 1^5$. Panel (a) shows the isola of $1^7 1^5$ MMO periodic orbits (dark red) with the 1^7 isola from Figure 12(a) (grey). Panels (b)–(d) show the marked periodic orbits $\tilde{\Gamma}_1$, $\tilde{\Gamma}_2$, $\tilde{\Gamma}_3$ and $\tilde{\Gamma}_4$ with Γ_ν .

6 Shilnikov homoclinic bifurcation involving MMOs

The recurrent dynamics shown in Section 5 is characterised by having a saddle-focus equilibrium p with a two-dimensional unstable manifold $W^u(p)$ and a one-dimensional stable manifold $W^s(p)$, together with a global return mechanism involving slow and fast episodes. Some orbits are reinjected to a neighborhood of p along $W^s(p)$ and spiral out along $W^u(p)$. This suggests the existence of a Shilnikov homoclinic bifurcation [19, 35] for nearby values of the parameters.

Koper and Gaspard introduced a three-dimensional model to analyze an electrochemical diffusion problem in which layer concentrations of electrolytic solutions fluctuate nonlinearly at an electrode [28, 29]; their model is known as the Koper model, and it is a subfamily of system (1). Koper and Gaspard suspected the existence of a Shilnikov homoclinic orbit, but were not able to find such an orbit in their model equations. The paper by Guckenheimer and Lizarraga [21] is entirely dedicated to the detection of the Shilnikov homoclinic orbit in the Koper model, which found for the specific parameter values

$$a = -0.2515348, \quad b = -1.650823, \quad c = 1, \quad \varepsilon = 0.01 \quad \text{and} \quad \nu \approx 0.023895. \quad (3)$$

They identified a homoclinic orbit in system (1) and then continued it in parameters until it lies in the submanifold in parameter space that corresponds to the Koper model. To find the

specific homoclinic orbit in system (1), Guckenheimer and Lizarraga extended the parameter space by introducing an extra parameter into the system, which parameterises the unstable manifold of p . They then applied numerical shooting to find a homoclinic orbit as a transverse intersection of the families of the stable and unstable manifolds of the curve of equilibria in the system. The homoclinic orbit is defined in the extended parameter space \bar{P} by an equation of the form $\psi = 0$, where $\psi : \bar{P} \mapsto \Sigma$ measures the difference between the end points of orbit segments of $W^u(p)$ and $W^s(p)$ in a suitable transverse section Σ .

We now show how this and other Shilnikov homoclinic orbits in system (1) can be identified more directly in a systematic way with a boundary value problem setup. The starting points are given by the MMOs from Section 5, more specifically those from the 1^7 isola. Since the MMO periodic orbits from the 1^7 isola approach p after the global return, it is logical to think that they may become a Shilnikov homoclinic orbit when parameters are changed in a suitable way. One may also think that it would be enough to continue the isola in one parameter to get close to a Shilnikov bifurcation. However, we find no transverse intersection between $W^u(p)$ and $W^s(p)$ when a single parameter is changed. This is because Γ_ν remains stable and trajectories on $W^u(p)$ converge to Γ_ν when $t \rightarrow \infty$, so they fail to connect back to p . The MMO periodic orbits from the 1^7 isola disappear in saddle-node bifurcations when they are continued in ν . Nevertheless, they still can be continued in a sequence of parameters and it is possible to identify in this way high-period MMO periodic orbits, which are candidates for nearby Shilnikov orbits.

To demonstrate this idea, we continue the 1^7 isola toward the parameter values (3), where it is known from [21] that a Shilnikov homoclinic orbit exists. Figure 17 shows in panel (a) the isola of MMO periodic orbits (cyan) when a , b , c and ε are as given by (3). Here the MMO periodic orbits are represented by their period T as a function of the parameter $\nu \in (0.006, 0.036)$. This isola is quite different from the 1^7 isola in Figure 13(a), and we point out two main differences: First of all, the number of SAOs changes along the isola in Figure 17(a) so that one can no longer speak of an isola of 1^7 MMO periodic orbits. Secondly, there are two (locally) high-period periodic orbits on the isola, which are candidates for intersections of $W^u(p)$ with $W^s(p)$. Panels (b)–(e) of Figure 17 show periodic orbits corresponding to the labelled points on the isola. The MMO periodic orbits (b) and (c) seem to spiral around $W^s(p)$, but they do not get close enough to p . The MMO periodic orbits (d) and (e), on the other hand, look like Shilnikov homoclinic orbits. They are local maxima of T on the isola at $\nu_d \approx 0.029496$ and $\nu_e \approx 0.027436$, respectively. Figures 17(d) and (e) show that the high periods are due to a very close passage near the saddle-focus p . We remark that the SAOs in (d) and (e) are so small that they are not visible due to the fast contraction toward p . Since we found two candidates for parameter values, we now set up a boundary value problem for finding homoclinic orbits. Specifically, we implement a Lin’s method approach [32, 36, 39] to detect codimension-one transverse intersections between $W^u(p)$ and $W^s(p)$. It is effectively the same method we use for detecting connecting canard orbits in Section 3, but now we consider $\pi_{13}^+(\widehat{W}_1)$ and the point $\widehat{W}^s(p)$, which are the corresponding intersection sets of $W^u(p)$ and $W^s(p)$ in Σ_3 . Moreover, we need to include a system parameter in the continuation in order to detect the intersection; see the appendix for more details.

Figure 18 shows this setup, where we start from the parameter values for point (d) in Figure 17(a), with a , b , c and ε as in (3) and $\nu = \nu_d$, and compute $W^u(p)$ and $W^s(p)$ up to Σ_3 . Panel (a) shows $W^u(p)$ (red) and $W^s(p)$ (blue) computed up to Σ_3 in the implementation of Lin’s method, where we included Γ_ν (green) for completeness. Note that Γ_ν is no longer attracting for these parameter values. The homoclinic bifurcation does not occur for $\nu =$

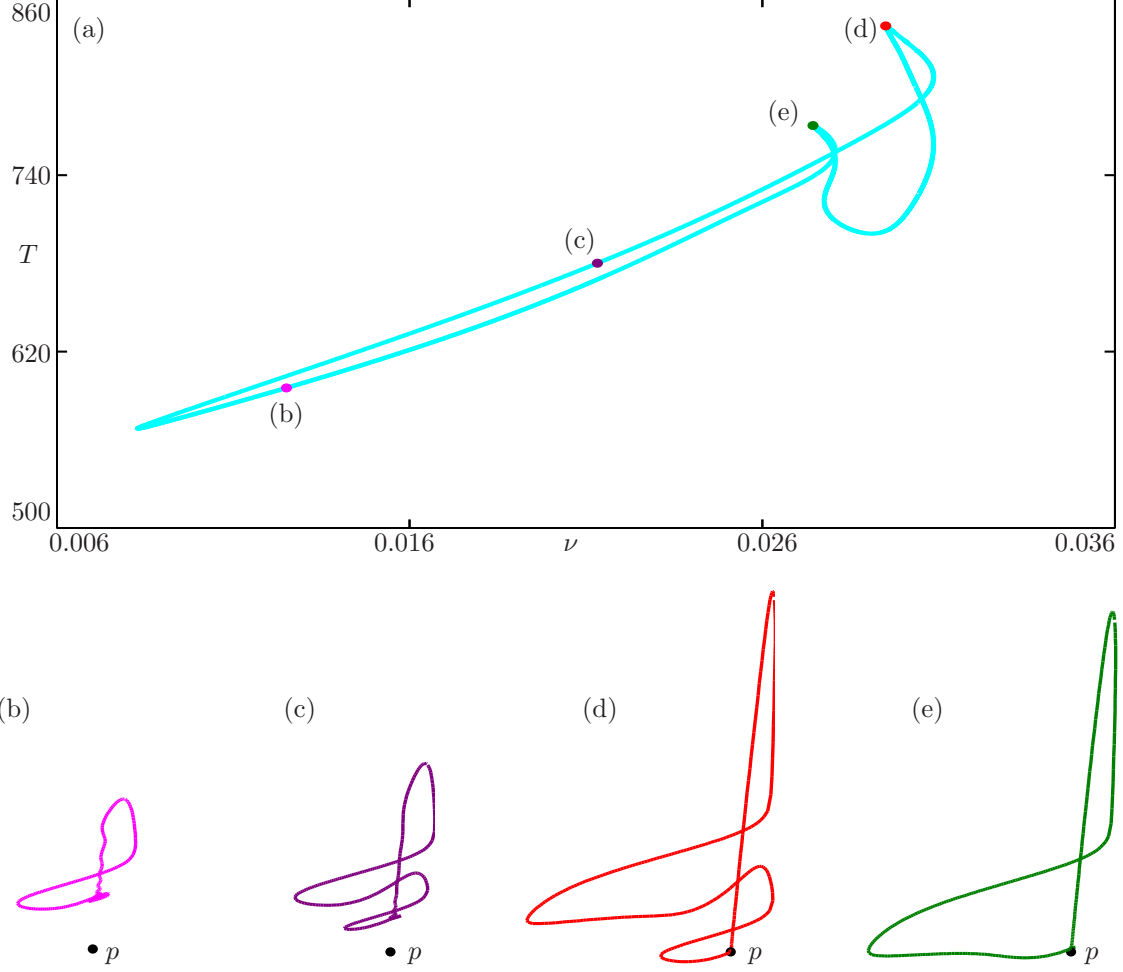


Figure 17: Isola of MMO periodic orbits for $a = -0.251348$, $b = -1.650823$, $c = 1$ and $\varepsilon = 0.01$, continued from the isola in Figure 12(a). Panels (b)–(e) show in (x, y, z) -space the orbits for the corresponding labeled dots in panel (a).

ν_d , but the intersection sets $\pi_{13}^+(\widehat{W}_1)$ and $\widehat{W}^s(p)$ are very close to each other already. In particular, the computed part of $W^u(p)$ includes a global return of orbits before this manifold intersects Σ_3 . Lin’s method provides a well-defined test function to detect the moment $\widehat{W}^s(p)$ lies on $\pi_{13}^+(\widehat{W}_1)$ as ν varies. The Shilnikov homoclinic orbit has been detected with our approach at $\nu = \nu_{\text{hom1}} \approx 0.023897$. The orbit on $W^u(p)$ that makes the connection with $W^s(p)$ is highlighted in Figure 18(a). Panel (b) shows the intersection sets $\pi_{13}^+(\widehat{W}_1)$ and $\widehat{W}^s(p)$ in Σ_3 of the computed piece of $W^u(p)$ and $W^s(p)$, respectively, for $\nu = \nu_{\text{hom1}}$. Note the spiralling of $\pi_{13}^+(\widehat{W}_1)$ around $\widehat{W}^s(p)$ and how $\pi_{13}^+(\widehat{W}_1)$ terminates at $\widehat{W}^s(p)$, as expected for a Shilnikov homoclinic bifurcation [1]. Figure 18(c) shows only the actual Shilnikov homoclinic orbit (gray) for $\nu = \nu_{\text{hom1}}$, obtained as the concatenation of the corresponding orbit segment of $W^u(p)$ and $W^s(p)$. The value $\nu_{\text{hom1}} \approx 0.023897$ we found agrees with the value of ν in (3), found by Guckenheimer and Lizarraga [21], up to an error of less than 10^{-6} , which is within the accuracy of an AUTO calculation. In addition, the orbit they found and the one we found have the same shape. Therefore, we conclude that the Shilnikov homoclinic orbit in Figure 18(c) is the one found in [21]. Also shown in Figure 18(c) is the periodic orbit Γ_ν , which is now of saddle type and still linked with the homoclinic orbit. In other words, this topological invariant persists even when Γ_ν is no longer attracting. Panel (d) shows an enlargement near the equilibrium

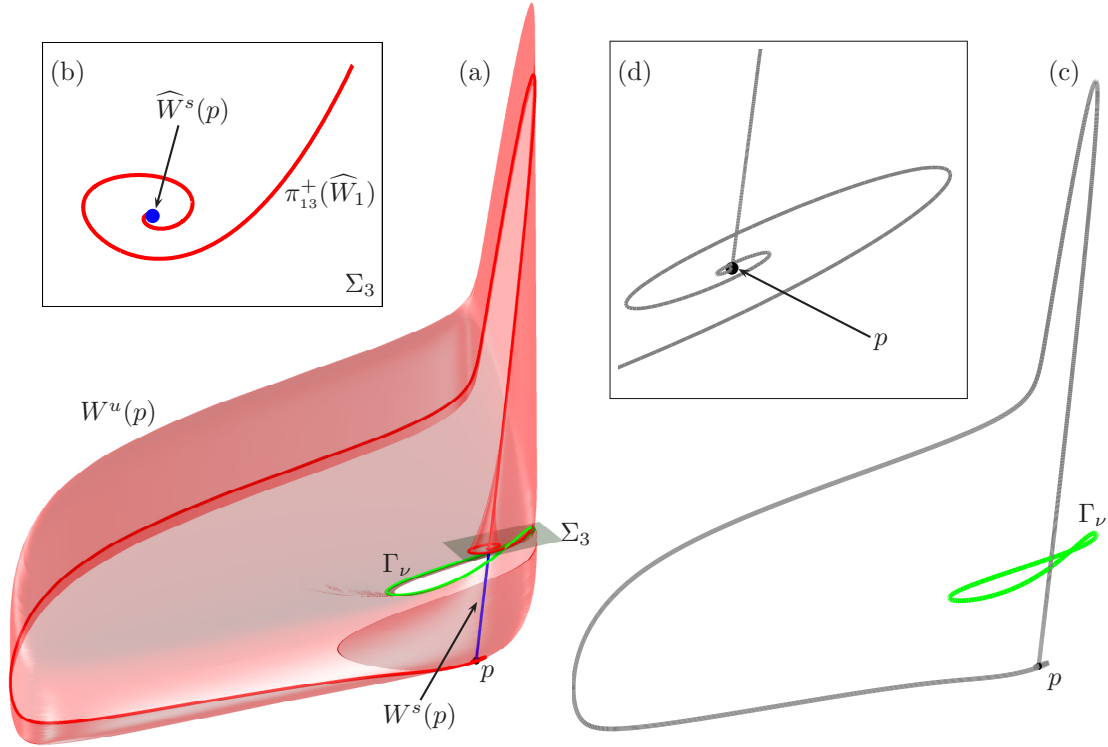


Figure 18: Shilnikov homoclinic orbit of system (1) for $a = -0.251348$, $b = -1.650823$, $c = 1$, $\varepsilon = 0.01$ and $\nu = \nu_{\text{hom1}} \approx 0.023897$. Panel (a) shows $W^u(p)$ and $W^s(p)$ computed up to section Σ_3 with Γ_ν . Panel (b) depicts the intersection sets of $W^u(p)$ and $W^s(p)$ with Σ_3 . Panel (c) shows the actual homoclinic orbit linked with Γ_ν , and the enlargement panel (d) highlights the spiralling behaviour around p .

point p , highlighting the spiraling dynamics on $W^u(p)$ near p .

The saddle quantity at $\nu = \nu_{\text{hom1}}$ is negative, which means that we are dealing with a chaotic Shilnikov bifurcation [43, 44]. Therefore, we expect to find more (chaotic) Shilnikov homoclinic orbits nearby. To illustrate this, we compute $W^u(p)$ and $W^s(p)$ up to Σ_3 for $\nu = \nu_e$ and, by setting up Lin's method again, we detect a different chaotic Shilnikov homoclinic orbit for $\nu = \nu_{\text{hom2}} \approx 0.023894$, which is at the same order of distance from ν in (3) as ν_{hom1} ; this homoclinic orbit is also linked with Γ_ν . Figure 19 illustrates the homoclinic orbit in panel (a) together with Γ_ν . Note that the shape of this new homoclinic orbit is completely different from the one at $\nu = \nu_{\text{hom1}}$, even though their corresponding ν -values are very close. An enlargement near p of the homoclinic orbit is shown in panel (b). Panel (c) of Figure 19 shows the same homoclinic orbit, this time coexisting with two saddle MMO periodic orbits Γ_b (black) and Γ_m (magenta) and Γ_ν (green). Panel (d) is an enlargement near p and Γ_ν . It shows that Γ_b approaches Γ_ν along its stable manifold $W^s(\Gamma_\nu)$ and then leaves the vicinity of Γ_ν along its unstable manifold $W^u(\Gamma_\nu)$. The orbits Γ_b and Γ_m lie on the isola from Figure 17(a) for $\nu = \nu_{\text{hom2}}$. Similarly, for $\nu = \nu_{\text{hom1}}$ there are two saddle MMO periodic orbits interacting with the corresponding Shilnikov homoclinic orbit and Γ_ν . This is a clear indicator of the existence of more complex dynamics involving, for instance, chaos in the form of a suspended horseshoe, homoclinic orbits to Γ_ν , interactions between more invariant objects and EtoP connections. We suspect the existence of a large chaotic attractor associated with the global return, as well as a small chaotic attractor associated with Γ_ν . The further study of this complex overall dynamics is an interesting challenge beyond the scope of this paper.

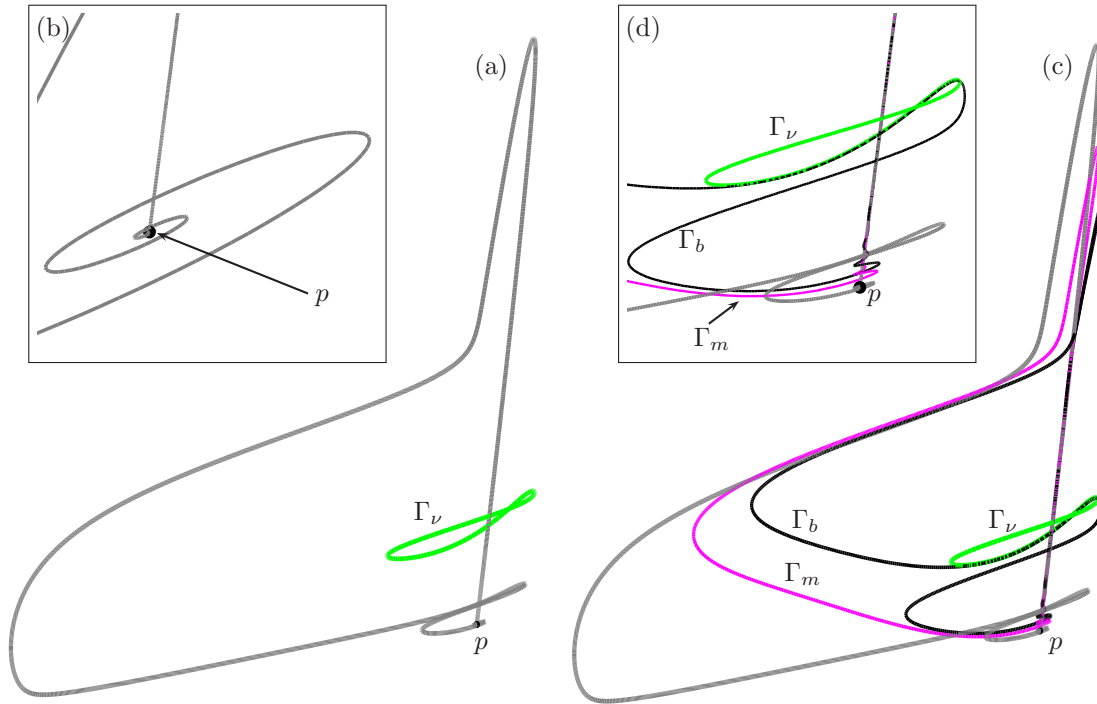


Figure 19: Shilnikov homoclinic orbit of system (1) for $a = -0.251348$, $b = -1.650823$, $c = 1$, $\varepsilon = 0.01$ and $\nu = \nu_{\text{hom}2} \approx 0.023894$. Panel (a) shows the homoclinic orbit (gray) with Γ_ν (green) on phase space, while panel (b) shows an enlargement of the orbit near p . Panel (c) shows the same homoclinic orbit and Γ_ν coexisting with the MMOs Γ_b and Γ_m (black and magenta, respectively), with an enlargement close to Γ_ν in panel (d).

7 Discussion

We studied invariant and slow manifolds in a three-dimensional normal form of the singular Hopf bifurcation from [7]. Specifically, we considered the interaction of the unstable manifold $W^u(p)$ of a saddle focus equilibrium p with the repelling slow manifold S_ε^r of system (1). We computed both local and global aspects of $W^u(p)$ and S_ε^r . By defining Poincaré maps between suitable cross sections we described and illustrated how the transition through a quadratic tangency between $W^u(p)$ and S_ε^r unfolds and what are the local and global consequences of this interaction. Its most immediate consequence is the dramatic growth of $W^u(p)$ with a small increase in ν . The unstable manifold $W^u(p)$ covers a much bigger region of phase space and the dynamics becomes intricate. Moreover, we found secondary interactions leading to jump-left/right canard orbits and MMOs. It is known that small-amplitude oscillations near a singular Hopf bifurcation are organised by a saddle-focus equilibrium and the small-amplitude limit cycle Γ_ν , born at the bifurcation. Here we described how the large-amplitude oscillations are created from the interaction between $W^u(p)$ and S_ε^r . A tangency provides a global return of $W^u(p)$ due to the presence of a second fold curve in the critical manifold, where the existence of connecting canard orbits plays an important role. We presented a global return mechanism that is a direct consequence of the interaction between $W^u(p)$ and S_ε^r . It produces secondary intersections between $W^u(p)$ and S_ε^r in a robust manner as ν varies, and gives rise to MMO periodic orbits close to $W^u(p)$ that are all linked with the periodic orbit Γ_ν , which is an attractor in this parameter regime. We found two such branches, which are isolas of MMO

periodic orbits with signatures 1^7 and $1^7 1^5$, respectively. Other combinations and different geometric mechanisms creating them may exist, but we did not pursue them in this paper.

We tracked the family of MMO periodic orbits in various parameters to find high-period periodic orbits near Shilnikov homoclinic bifurcations of MMOs. This allowed us to find two homoclinic bifurcation points and the associated Shilnikov homoclinic orbits by a Lin's method approach, one of which had already been identified in [21] by a different approach. We also found evidence of further homoclinic bifurcation points in parameter space, which arise from different interactions between the manifolds $W^u(p)$ and S_ε^r . The MMOs from the $1^7 1^5$ isola can be continued in parameters and should provide additional Shilnikov homoclinic orbits. There are also indications of EtoP connections and homoclinic orbits to Γ_ν in system (1), which we suspect to be organising centres for complicated dynamics. Finally, for some parameter regimes, Γ_ν is no longer the boundary of $W^u(p)$; hence, the geometry of $W^u(p)$ is expected to change and give rise to interesting dynamics. The periodic orbit Γ_ν undergoes period-doubling bifurcations, where the period-doubled periodic orbits could provide different MMO signatures if the interaction between $W^u(p)$ and S_ε^r persists. A detailed analysis of the overall structure of other Shilnikov homoclinic bifurcations in system (1) and of different scenarios for the occurrence of complex dynamics is left for future research.

The interaction of S_ε^r with $W^u(p)$ dramatically changes the overall dynamics in system (1) by making the global return available after the tangency. The recurrent objects found as a result, including different types of MMOs, are structurally stable. Since the tangency between S_ε^r and $W^u(p)$ is a generic phenomenon one should expect to find this transition and the ensuing recurrent dynamics in other multiple-time-scale systems with the respective geometric ingredients. In particular, because our study concerns a normal form of a singular Hopf bifurcation [7, 22], the dynamics described in this paper should occur in slow-fast systems with a singular Hopf bifurcation and a global return mechanism; the Koper model for idealised chemical reactions [27] is a specific example, and other good candidates might be models for calcium dynamics and for neuron spiking and bursting. An alternative way of looking for the dynamics discussed here would be to identify a slow-fast Shilnikov bifurcation point and other codimension-one homoclinic bifurcations arising near a tangency of a slow manifold with a global invariant manifold of a saddle equilibrium or periodic orbit.

Finally, the study presented here demonstrates the strength and versatility of our approach of continuing orbit segments in a boundary value problem setup as a tool for studying global dynamical properties and new phenomena in slow-fast systems. Importantly, the boundary value problem remains well posed despite the extreme sensitivity with respect to initial conditions. We expect that this computational approach will be fruitful also for further investigation of some of the issues raised above.

Acknowledgments

We thank John Guckenheimer for fruitful discussions about global return mechanisms, Martin Wechselberger for his suggestions about the role of slow manifolds in the dynamics of system (1), and Andy Hammerlindl and Carlos Vasquez for discussions about horseshoe structures during their visits to The University of Auckland.

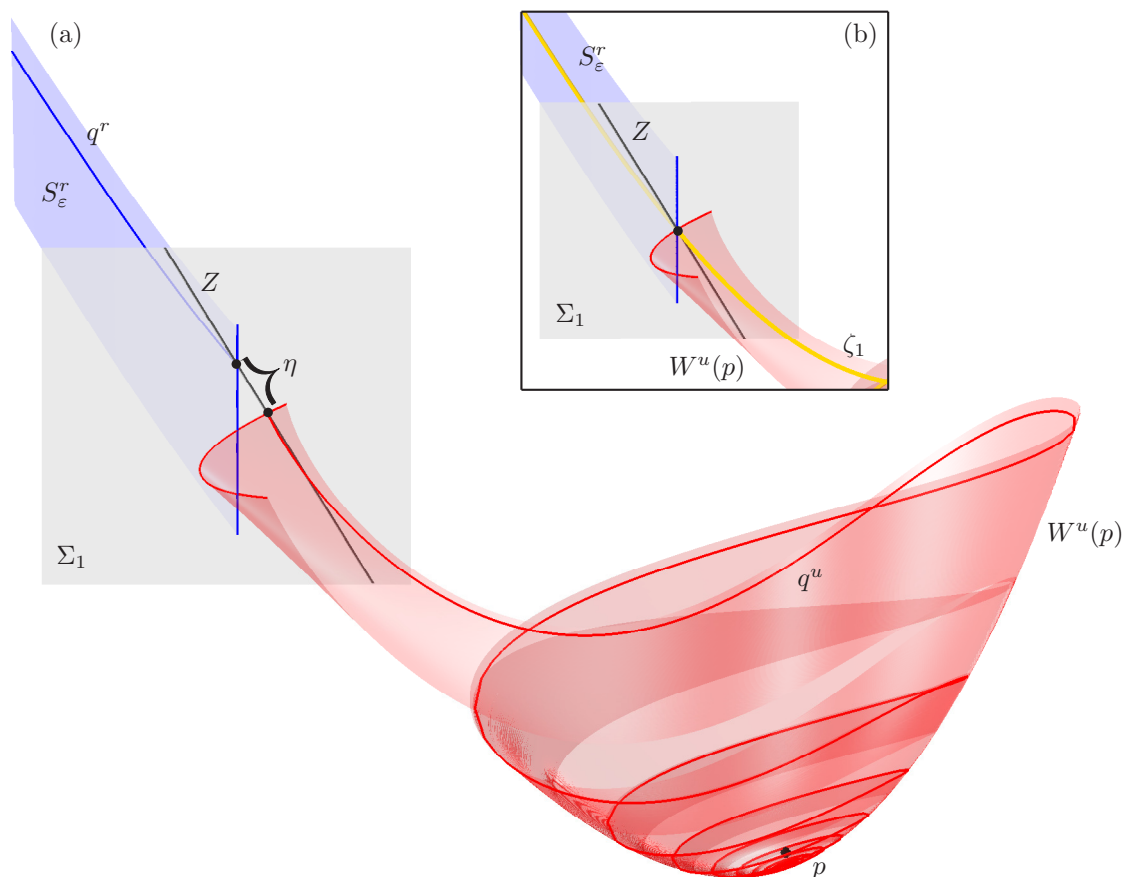


Figure 20: Illustration of Lin's method applied to system (1) with $\nu = 0.00712$. Panel (a) shows a general view of S_ε^r (blue) and $W^u(p)$ (red) computed up to section Σ_1 , including the orbits q^r (blue) and q^u (red), on S_ε^r and $W^u(p)$ respectively, whose end points define the Lin gap η along the Lin space Z in Σ_1 . Panel (b) shows the Lin gap η closed, so that the connecting canard orbit ζ_1 (gold) is detected.

Appendix: Lin's method approach for detecting connecting canard orbits

The existence of connecting canard orbits that arise from the intersection between $W^u(p)$ and S_ε^r is crucial for the global return mechanism described in this paper. Here we discuss some of the techniques we use to find these connecting canard orbits. We calculate $W^u(p)$ and S_ε^r via the continuation of a two-point boundary value problem setup with the package AUTO [11]. The manifolds are then computed as families of orbit segments that are solutions of this boundary value problem; we refer to [30] for a general background. Once the data is generated in AUTO we export it into MATLAB, where we process the data and produce the figures.

To detect the connecting canard orbits we use a Lin's method approach [32, 36, 39]. Figure 20 shows an illustration of the Lin's method setup for finding the connecting canard orbit ζ_1 of system (1) for $\nu = 0.00712$; compare Figure 4. Panel (a) shows a global view, where a part of $W^u(p)$ and a part of S_ε^r are computed up to Σ_1 ; the orbits on $W^u(p)$ are solutions of a two-point boundary value problem, where one end point lies on a one-dimensional fundamental domain in the linear unstable eigenspace $E^u(p)$ close to p , and the other end point lies on Σ_1 ; orbit segments on S_ε^r have one end point on a (one-dimensional) line segment $L^r \subset S^r$ transverse to the flow, where S^r is the repelling middle sheet of the critical manifold S of system (1), and

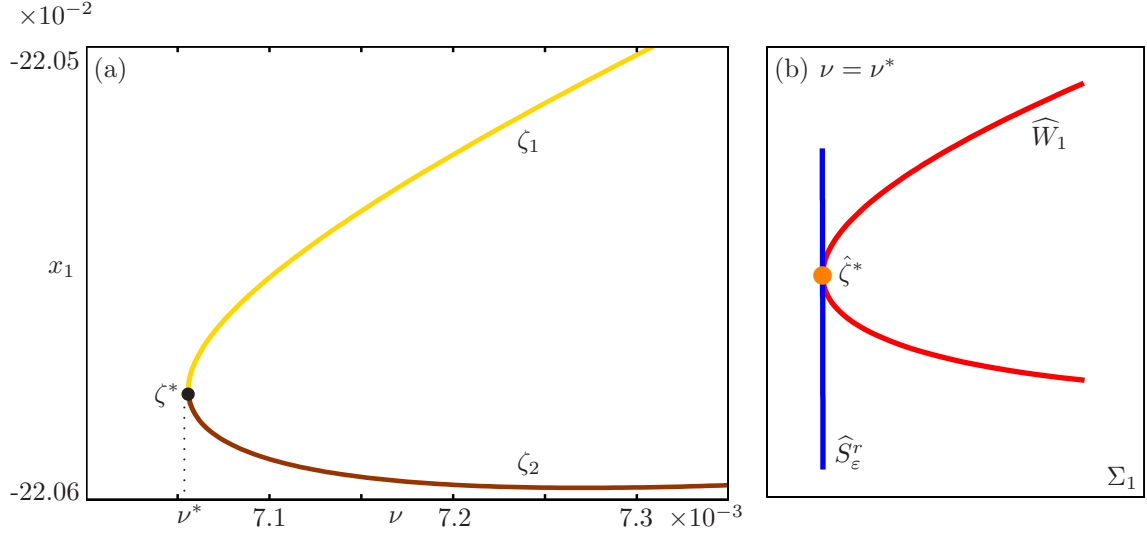


Figure 21: Continuation of a connecting canard orbit. Panel (a) shows a curve in the (ν, x_1) -plane, where x_1 is the x -coordinate of the end point on Σ_1 of the connecting canard orbit. Panel (b) shows a tangency between S_ε^r (blue) and $W^u(p)$ (red) on Σ_1 for $\nu = \nu^*$, which produces the connecting canard orbit ζ^* (orange dot).

their other end point lies on Σ_1 . We compute a connecting canard orbit as a connection from p to L^r . We select initial orbit segments $q^r \subset S_\varepsilon^r$ and $q^u \subset W^u(p)$, and use their end points in Σ_1 to define a one-dimensional Lin space Z . We now continue q^r and q^u in such a way that the direction defined by their end points in Σ_1 is that given by the fixed direction Z . The signed distance η between these end points is a well defined test function for detecting the connecting canard orbits; it is referred to as the Lin gap. A connecting canard orbit corresponds to a zero of the Lin gap η . Figure 20(b) shows the situation when $\eta = 0$, for which the concatenation of q^u and q^r forms the connecting canard orbit ζ_1 , shown in gold. Note that the other connecting canard orbit ζ_2 can be obtained as a second zero of the Lin gap η . The same Lin's method approach can be applied for finding secondary and further intersections between $W^u(p)$ and S_ε^r , this time considering orbit segments on $W^u(p)$ with a global return.

Once a connecting canard orbit is found, we switch the setup and define the connecting canard orbit as a single orbit segment that can be continued in parameters as a solution of system (1); here, one end point lies on the fundamental domain of $W^u(p)$ and the other end point lies on L^r . Note that we can still track their intersection with Σ_1 . Figure 21(a) shows the x -coordinate of the end point of the connecting canard orbit on Σ_1 as a function of ν ; this x -value can be taken either as the end point of the orbit segment q^u or the start point of the orbit segment q^r . For sufficiently large ν in panel (a), there exist two connecting canard orbits ζ_1 and ζ_2 that correspond to the upper and lower branch of the curve shown in gold and brown, respectively. For these ν -values, the intersection between $W^u(p)$ and S_ε^r is transverse; see Figure 4 as a reference. The two branches join at a fold point at $\nu = \nu^* \approx 0.00705579$, which corresponds to a quadratic tangency between $W^u(p)$ and S_ε^r along a single orbit. This tangency gives rise to the connecting canard orbit ζ^* ; see Figure 3. For $\nu < \nu^*$, there is no interaction between $W^u(p)$ and S_ε^r ; compare Figure 2. A first tangency between \widehat{W}_1 and $\widehat{S}_\varepsilon^r$ in the section Σ_1 and the connecting canard ζ^* are shown in Figure 21(b). Note that this is the case $\nu = \nu^*$ from Figure 3. Secondary connecting canard orbits and the secondary tangency at $\nu = \nu^{**} \approx 0.00715523$ were detected as folds with the same approach.

References

- [1] P. AGUIRRE, B. KRAUSKOPF AND H. M. OSINGA, *Global invariant manifolds near a Shilnikov homoclinic bifurcation*, Journal of Computational Dynamics, 1 (2014), pp 1–38.
- [2] V. I. ARNOL'D, ED., *Encyclopedia of Mathematical Sciences: Dynamical Systems V*, Springer-Verlag, Berlin, New York, 1994.
- [3] R. BERTRAM, M. J. BUTTE, T. KIEMEL AND A. SHERMAN, *Topological and phenomenological classification of bursting oscillations*, Bulletin of Mathematical Biology, 57(3) (1995), pp 413–439.
- [4] C. BONATTI, L. DIAZ AND M. VIANA, *Dynamics Beyond Uniform Hyperbolicity: A Global Geometric and Probabilistic Approach*, Encyclopedia Math. Sci., Springer, 2004.
- [5] B. BRAAKSMA, *Singular Hopf Bifurcation in systems with fast and slow variables*, J. Nonlinear Sci. Vol. 8 (1998), pp. 457–490 .
- [6] M. BRØNS, M. KRUPA, AND M. WECHSELBERGER, *Mixed mode oscillations due to the generalized canard phenomenon*, Fields Inst. Commun., 49 (2006), pp. 39–63.
- [7] M. DESROCHES, J. GUCKENHEIMER, B. KRAUSKOPF, C. KUEHN, H. M. OSINGA AND M. WECHSELBERGER, *Mixed-mode oscillations with multiple time scales*, SIAM Review 54(2) (2012), pp. 211–288.
- [8] M. DESROCHES, B. KRAUSKOPF, AND H. M. OSINGA, *The geometry of slow manifolds near a folded node*, SIAM J. Appl. Dyn. Syst., 7 (2008), pp. 1131–1162.
- [9] M. DESROCHES, B. KRAUSKOPF, AND H. M. OSINGA, *Mixed-mode oscillations and slow manifolds in the self-coupled FitzHugh-Nagumo system*, Chaos, 18 (2008), 015107.
- [10] M. DESROCHES, B. KRAUSKOPF AND H. M. OSINGA, *Numerical continuation of canard orbits in slow-fast dynamical systems*, Nonlinearity 23(3) (2010), pp. 739–765.
- [11] E. J. DOEDEL AND B. E. OLDEMAN, *AUTO-07p: Continuation and bifurcation software for ordinary differential equations*, with mayor contribution from A. C. Champneys, F. Dercole, T. F. Fairgrieve, Yu. A. Kuznetsov , R. C. Paffenroth, B. Sandstede, X. J. Wang and C. Zhang, 2012. Available via <http://cmvl.cs.concordia.ca/auto/>.
- [12] J. P. ENGLAND, B. KRAUSKOPF, AND H. M. OSINGA, *Computing two-dimensional global invariant manifolds in slow-fast systems*, Internat. J. Bifur. Chaos Appl. Sci. Engrg., 17 (2007), pp. 805–822.
- [13] N. FENICHEL, *Persistence and smoothness of invariant manifolds for flows*, Indiana Univ. Math. J., 21 (1971), pp. 193–225.
- [14] N. FENICHEL, *Geometric singular perturbation theory for ordinary differential equations*, J. Differential Equations, 31 (1979), pp. 53–98.
- [15] J. GINOUX, B. ROSSETTO, L. CHUA, *Slow invariant manifolds as curvature of the flow of dynamical systems*, Int. J. Bif. Chaos, 18(11) (2008), pp. 3409–3430.
- [16] J. GUCKENHEIMER, *Singular Hopf Bifurcation in systems with two slow variables*, SIAM J. Appl. Dyn. Syst., 7 (2008), pp. 1355–1377.

- [17] J. GUCKENHEIMER, *Return maps of folded nodes and folded saddle-nodes*, Chaos, 18 (2008), 015108.
- [18] J. GUCKENHEIMER AND R. HAIDUC, *Canards at folded nodes*, Moscow Math. J., 25 (2005), pp. 91–103.
- [19] J. GUCKENHEIMER AND P. HOLMES, *Nonlinear Oscillations, Dynamical Systems and Bifurcations of Vector Fields*, Springer-Verlag, Berlin, New York, 1983.
- [20] J. GUCKENHEIMER AND C. KUEHN, *Computing slow manifolds of saddle type*. SIAM J. Appl Dyn. Sys, 8(3) (2009), pp 854–879.
- [21] J. GUCKENHEIMER, I. LIZARRAGA, *Shilnikov homoclinic bifurcation of mixed-mode oscillations*, SIAM J. Appl. Dyn. Syst., 14 (2015), pp. 764–786.
- [22] J. GUCKENHEIMER, P. MEERKAMP, *Unfoldings of singular Hopf bifurcation*, SIAM J. Appl. Dyn. Syst., 11 (2012), pp. 1325–1359.
- [23] A. HARO, M. CANADELL, J. FIGUERAS, A. LUQUE AND J. MONDELO, *The parameterization method for invariant manifolds*, Appl. Math. Sci. Ser., vol. 195, Springer, New York, 2016.
- [24] IZHIKEVICH E. M., *Neural excitability, spiking and bursting*, International Journal of Bifurcation and Chaos, 10 (2000), pp. 1171–1266.
- [25] IZHIKEVICH E. M. , *Dynamical Systems in Neuroscience: The Geometry of Excitability and Bursting*, MIT Press, Cambridge, 2007.
- [26] C. K. R. T. JONES, *Geometric singular perturbation theory*, in J. Russell (Ed.), Dynamical Systems (Montecatini Terme, 1994), Springer-Verlag, Berlin, New York, 1995, pp. 44–118.
- [27] M. T. M. KOPER, *Bifurcations of mixed-mode oscillations in a three-variable autonomous Van der Pol-Duffing model with a cross-shaped phase diagram*, Phys. D, 80 (1995), pp. 72–94.
- [28] M. T. M. KOPER AND P. GASPARD, *Mixed-mode oscillations in a simple model of an electrochemical oscillator*, J. Phys. Chem., 95 (1991), pp. 4945–4947.
- [29] M. T. M. KOPER AND P. GASPARD, *The modelling of mixed-mode and chaotic oscillations in electrochemical systems*, J. Chem. Phys., 96 (1992), pp. 7797–7813.
- [30] B. KRAUSKOPF AND H. M. OSINGA, *Computing invariant manifolds via the continuation of orbit segments*, in B. Krauskopf, H.M. Osinga and J. Galán-Vioque (Eds.), Numerical Continuation Methods for Dynamical Systems: Path following and boundary value problems, Springer-Verlag, 2007, pp. 117–154.
- [31] B. KRAUSKOPF, H. M. OSINGA, E. J. DOEDEL, M. HENDERSON, J. GUCKENHEIMER, A. VLADIMIRSKY, M. DELLNITZ, AND O. JUNGE, *A survey of methods for computing (un)stable manifolds of vector fields*, Internat. J. Bifur. Chaos Appl. Sci. Engrg., 15 (2005), pp. 763–792.
- [32] B. KRAUSKOPF AND T. RIEß, *A Lin’s method approach to finding and continuing heteroclinic connections involving periodic orbits*, Nonlinearity 21 (2008), pp. 1655–1690.

- [33] M. KRUPA AND M. WECHSELBERGER, *Local analysis near a folded saddle-node singularity*, J. Differential Equations, 248 (2010), pp. 2841–2888.
- [34] C. KUEHN, *Multiple Time Scale Dynamics*, Appl. Math. Sci. Ser., vol. 191, Springer, New York, 2015.
- [35] YU. A. KUZNETSOV, *Elements of Applied Bifurcation Theory*, 3rd ed., Springer-Verlag, Berlin, New York, 2004.
- [36] LIN X-B, *Using Melnikov's method to solve Shilnikov's problem*, Proc. R. Soc. Edinb A 116 (1990), pp. 295–325.
- [37] A. MILIK AND P. SZMOLYAN, *Multiple time scales and canards in a chemical oscillator*, in C. Jones and A. Khibnik (Eds.), *Multiple-Time-Scale Dynamical Systems*, IMA Vol. Math. Appl. 122, Springer-Verlag, Berlin, New York, 2001, pp. 117–140.
- [38] J. MOEHLIS, *Canards for a reduction of the Hodgkin-Huxley equations*, Journal of Mathematical biology, 52(2) (2006), pp. 141–153.
- [39] B. OLDEMAN, A. R. CHAMPNEYS AND B. KRAUSKOPF, *Homoclinic branch switching: A numerical implementation of Lin's method*, Internat. J. Bifur. Chaos, 13(10) (2003), pp. 2977–2999.
- [40] J. PALIS AND W. DE MELO, *Geometric Theory of Dynamical Systems*, Springer-Verlag, New York, Heidelberg, Berlin, 1982.
- [41] C. PUCH, *The closing lemma*, Amer. J. Math. 89 (1967), pp 956–1009.
- [42] C. PUGH, C. ROBINSON, *The C^1 closing lemma, including Hamiltonians*, Ergod. Th. Dynam. Sys. 3 (1983), pp 261–313.
- [43] L.P. SHILNIKOV, *A case of the existence of a denumerable set of periodic motions*, Sov. Math. Dokl., 6 (1965), 163–166.
- [44] L.P. SHILNIKOV, *A contribution of the problem of the structure of an extended neighbourhood of a rough state to a saddle-focus type*, Math. USSR-Sb, 10 (1970), 91–102.
- [45] S. SMALE, *Differentiable dynamical systems*, Bull. Amer Math. Soc. 73 (1967), pp. 747–817.
- [46] P. SZMOLYAN AND M. WECHSELBERGER, *Canards in \mathbb{R}^3* , J. Differential Equations, 177 (2001), pp. 419–453.
- [47] M. WECHSELBERGER, *Existence and bifurcation of canards in \mathbb{R}^3 in the case of a folded node*, SIAM J. Appl. Dyn. Syst., 4 (2005), pp. 101–139.